

# Reconstructing WIMP properties through an interplay of signal measurements in direct detection, Fermi-LAT, and CTA searches for dark matter

Leszek Roszkowski,<sup>a,b</sup> Enrico Maria Sessolo,<sup>a</sup>  
Sebastian Trojanowski<sup>a</sup> and Andrew J. Williams<sup>a</sup>

<sup>a</sup>National Centre for Nuclear Research,  
Hoża 69, 00-681 Warsaw, Poland

<sup>b</sup>Department of Physics and Astronomy, University of Sheffield,  
Sheffield S3 7RH, United Kingdom

E-mail: [L.Roszkowski@sheffield.ac.uk](mailto:L.Roszkowski@sheffield.ac.uk), [enrico.sessolo@ncbj.gov.pl](mailto:enrico.sessolo@ncbj.gov.pl),  
[sebastian.trojanowski@ncbj.gov.pl](mailto:sebastian.trojanowski@ncbj.gov.pl), [andrew.williams.2009@live.rhul.ac.uk](mailto:andrew.williams.2009@live.rhul.ac.uk)

**Abstract.** We examine the projected ability to reconstruct the mass, scattering, and annihilation cross section of dark matter in the new generation of large underground detectors, XENON-1T, SuperCDMS, and DarkSide-G2, in combination with diffuse gamma radiation from expected 15 years of data from Fermi-LAT observation of 46 local spiral dwarf galaxies and projected CTA sensitivity to a signal from the Galactic Center. To this end we consider several benchmark points spanning a wide range of WIMP mass, different annihilation final states, and large enough event rates to warrant detection in one or more experiments. As previously shown, below some 100 GeV only direct detection experiments will in principle be able to reconstruct WIMP mass well. This may, in case a signal at Fermi-LAT is also detected, additionally help restricting  $\sigma v$  and the allowed decay branching rates. In the intermediate range between some 100 GeV and up a few hundred GeV, direct and indirect detection experiments can be used in complementarity to ameliorate the respective determinations, which in individual experiments can at best be rather poor, thus making the WIMP reconstruction in this mass range very challenging. At large WIMP mass,  $\sim 1$  TeV, CTA will have the ability to reconstruct mass, annihilation cross section, and the allowed decay branching rates to very good precision for the  $\tau^+\tau^-$  or purely leptonic final state, good for the  $W^+W^-$  case, and rather poor for  $b\bar{b}$ . A substantial improvement can potentially be achieved by reducing the systematic uncertainties, increasing exposure, or by an additional measurement at Fermi-LAT that would help reconstruct the annihilation cross section and the allowed branching fractions to different final states.

---

## Contents

<b>1</b>	<b>Introduction</b>	<b>1</b>
<b>2</b>	<b>Reconstructing a signal</b>	<b>3</b>
2.1	Signal in underground detectors	3
2.2	Gamma-ray signals from dwarf spheroidal galaxies and the Galactic Center	4
2.2.1	Likelihood function for Fermi-LAT dSphs	5
2.2.2	Likelihood function for CTA	6
<b>3</b>	<b>Benchmark points and scanning methodology</b>	<b>8</b>
<b>4</b>	<b>Discussion of results</b>	<b>11</b>
<b>5</b>	<b>Summary and conclusions</b>	<b>22</b>

---

## 1 Introduction

In recent years several experiments have progressively put the paradigm of the weakly interactive massive particle (WIMP) as a cold dark matter (DM) to an increasing test. Currently the strongest bounds on the spin-independent WIMP-proton scattering cross section,  $\sigma_p^{\text{SI}}$ , have been achieved in the Xenon-based underground detector LUX [1, 2] which improved the previous best limit of XENON100 [3]. For WIMP mass in the range  $10 - 100 \text{ GeV}$  the limit is about  $\sigma_p^{\text{SI}} \lesssim 10^{-45} \text{ cm}^2$  at the 90% C.L., and it becomes weaker for larger mass. While underground detectors have also provided bounds on the spin-dependent cross section [4–6], the strongest limits on the scattering to the proton,  $\sigma_p^{\text{SD}} \lesssim 10^{-40} \text{ cm}^2$ , have been determined indirectly in neutrino telescopes [7–9]. As for measurements of the present-day DM annihilation cross section times WIMP relative velocity,  $\sigma v$ , which, following the convention used in the literature, we will refer to as simply the annihilation cross section, the strength of the upper bounds also depends on the WIMP mass. For  $m_\chi < 1 \text{ TeV}$  the most stringent limit comes from the Fermi-LAT Collaboration in the 6-year data from observation of 15 dwarf spheroidal satellite galaxies of the Milky Way (dSphs) [10] while for  $m_\chi \gtrsim 1 \text{ TeV}$  from observation of the Galactic Center (GC) with the air Cherenkov telescope H.E.S.S. [11].

With experiment probing deeper and deeper into plausible regions of WIMP cross sections, it is interesting to investigate to what extent a detection of a genuine WIMP signal in one or more experiments will allow one to actually reconstruct the WIMP mass and other properties. This issue will be addressed in the present paper.

The reconstruction abilities in direct detection underground experiments have been extensively studied [12–22], leading to the conclusion that a determination of DM particle properties from the signal should be achievable only in the relatively low WIMP mass range  $m_\chi \lesssim 100 \text{ GeV}$ . As regards the reconstruction of the DM properties from indirect detection experiments, studies were performed for Fermi-LAT, in putative data from the GC [23, 24], showing good accuracy in reconstructed mass below  $\sim 200 \text{ GeV}$  for large signals. Reconstruction of the DM properties from a spectral analysis of a putative strong signal in dSphs was performed in [25]. Moreover, in [26] the WIMP mass and annihilation cross section were also reconstructed from the real Fermi-LAT Galactic Center Excess data, under the assumption that it originates from DM annihilation.

As regards a complementary use of direct and indirect detection searches for WIMP reconstruction, an early study was performed in [27] where an interplay between expected XENON100

sensitivity and projected Fermi-LAT data from the GC was investigated at  $m_\chi \lesssim 50$  GeV. More recent studies of the interplay of the projected sensitivity of XENON-1T [28] and IceCube on reconstruction of the DM properties can be found in [29] and [30] (see also [31–34] for further studies on related topics).

We believe that, with much new available data and forthcoming new experiments, it is now an opportune time to update and enhance such analyses. For definiteness, in this paper we will focus on direct detection measurements of  $\sigma_p^{\text{SI}}$  – and will neglect  $\sigma_p^{\text{SD}}$  as typically giving a subdominant signal rate – and on realistic projected measurements at Fermi-LAT and the Cherenkov Telescope Array (CTA) [35] of the diffuse gamma radiation. We will not consider neutrino flux data nor antimatter (positron, antiproton, antideuteron) data, the latter of which are prone to large astrophysical uncertainties. Finally, we will not in this paper assume any positive information from the LHC or any future collider, like ILC or FCC. Indeed, detecting in a collider a WIMP-like particle would not necessarily imply that it actually comprises DM as such a particle could be unstable on a cosmological time scale.

From the theoretical point of view, increasing attention has recently been given to WIMPs with mass at the 1 TeV scale, which are a prediction of several models. For example, in models with GUT-unified supersymmetry, the most statistically significant region is an almost pure higgsino with  $m_\chi \sim 1$  TeV uniformly over wide ranges of the parameter space (see, e.g., [36] and references therein). It emerges in global analyses as a robust solution most naturally implied by primarily the 125 GeV mass value of the Higgs boson and the correct relic abundance. The  $\sim 1$  TeV higgsino features the present-day  $\sigma v$  around the “canonical” thermal expectation value of  $\sim 10^{-26}$  cm<sup>3</sup>/s, but is not uncommon to find regions of the parameter space where  $\sigma v$  can be as high as  $2 \times 10^{-25}$  cm<sup>3</sup>/s. At the same time, because of its very large higgsino component,  $\sigma_p^{\text{SI}}$  is typically in the range of  $10^{-46}$ – $10^{-45}$  cm<sup>2</sup>. Other models [37–39], also based on supersymmetry, can feature as the DM particle a 2–3 TeV wino, which features promising indirect detection prospects (see, e.g., [40]).

The intrinsic characteristics of this type of heavy candidates give reasons for optimism when it comes to the DM detection prospects in the immediate future. Tonne-scale underground detectors like LUX, XENON-1T [28] or LZ [41], based on Xe as a target, or even larger detectors based on Ar, like the proposed DarkSide-G2 [42] should just about cover the above-mentioned expected range for  $\sigma_p^{\text{SI}}$ . At the same time, it has been shown in several analyses [43–49], including one by some of us, that CTA is bound to reach unprecedented sensitivity to  $\sigma v$  for WIMPs with a mass in the TeV regime.

On the other hand, there is also a chance that a discovery will point to a WIMP with mass much less than a TeV. Indeed, this is what the possible signal excess at the GC that emerged in Fermi-LAT data a few years ago [50, 51] might be hinting at.<sup>1</sup> In that case, some recent studies have shown that the signal can be fitted by WIMPs whose  $\sigma v$  is around the canonical thermal value and the mass in the range 20 – 40 GeV (see, e.g., [26]) or 100 – 200 GeV (e.g., [53–57]), depending on the annihilation final state. For a WIMP with these characteristics, then, the most likely venue for discovery is at the moment given by Fermi-LAT. The Collaboration will continue analyzing data from dSphs, as more of these objects are discovered. In this paper we consider projected data in a hypothetical 15 year 46 dSphs analysis, which should improve the discovery reach in the low WIMP mass region.

There are some insurmountable barriers plus several sources of uncertainty that can interfere with the ability to reconstruct the correct WIMP mass, scattering, or annihilation cross section. As pertains to direct detection, particularly troubling is the fact that, for  $m_\chi \gtrsim 100$  GeV, event spectra become basically independent of  $m_\chi$ . Additionally there are uncertainties in the density

---

<sup>1</sup>However, a non-DM explanation has recently been proposed [52].

and velocity distribution of the DM in the galactic halo [58–62], and uncertainties in the detectors’ response. For indirect detections based on gamma rays from the GC, in addition to the above-mentioned uncertainties associated to the halo and its profile [63–67] there are also uncertainties in the cosmic-ray flux and in how the molecular clouds affect secondary gamma-ray emission. For dSphs, uncertainties in the  $J$ -factors can play an important role.

Assuming a genuine signal is detected in one or more experiment, direct or in the diffuse gamma ray mode, and given a realistic assessment of the current and future uncertainties, the questions we want to address in this paper are the following:

- How well can the regions of  $(m_\chi, \sigma_p^{\text{SI}})$  and  $(m_\chi, \sigma v)$  be determined by direct detection and gamma ray experiments, respectively, as well as by a complementary use of both to help disentangle possible degeneracies?
- How well can WIMP mass reconstruction be achieved in the gamma-ray experiments Fermi-LAT and CTA?
- How well can Fermi-LAT and CTA do in WIMP annihilation final state reconstruction?
- What are the challenges and possible obstacles to obtain improved results?

Our strategy will be as follows. We will assume some “true” DM WIMP by specifying its mass and other properties relevant to the type of measurement under consideration. For instance, in direct detection we will specify  $m_\chi$  and  $\sigma_p^{\text{SI}}$ . We will then generate a MC sample of possible other configurations which could mimic the signal from the assumed “true” DM WIMP. We emphasize that in this paper we will not be assuming any particle physics model or scenario. For this reason we will therefore not be imposing any limits from colliders nor from the relic abundance of dark matter.

The paper is organized as follows. In Sec. 2 we review the formalism for generating a mock signal in several selected direct and indirect detection experiments. We consider different nuclear targets for direct detection, and for indirect detection we consider gamma rays from dSphs and the GC. We conclude the section by presenting the explicit form of the likelihood functions. In Sec. 3 we describe the selected benchmark points that will generate the signals to fit and the scanning methodology. We present the reconstruction results in Sec. 4, and we conclude in Sec. 5.

## 2 Reconstructing a signal

We proceed to define the mock signals we will be trying to reconstruct to a  $\sim 2\sigma$  precision. As was mentioned in Sec. 1, we focus in this paper on the measurements of  $\sigma_p^{\text{SI}}$  in direct detection search experiments and of  $\sigma v$  and gamma-ray spectra in Fermi-LAT and CTA. We leave an analysis of other experimental modes to future work.

### 2.1 Signal in underground detectors

Experiments like XENON, LUX, DarkSide [68], SuperCDMS [69], and other, which are based on a specific fiducial volume of some target material placed in deep underground and well shielded detectors, measure the nuclear recoil differential rate  $dR/dE_R$  of the struck nucleon.

Following several papers [12–22] that performed similar analyses we parametrize the recoil energy in terms of a set of input parameters,  $\{p\}_{\text{DD}} = \{m_\chi, \sigma_p^{\text{SI}}, v_0, v_{\text{esc}}, \rho_0\}$ , where  $v_0$  is the circular



velocity of the DM halo,  $v_{\text{esc}}$  is the Galactic escape velocity at the Sun’s position, and  $\rho_0$  is the local DM density. Explicitly one gets

$$\frac{dR}{dE_R} = \frac{\sigma_p^{\text{SI}}}{2m_\chi \mu_{\chi p}^2} A^2 F_N^2(E_R) \mathcal{G}(v_{\text{min}}, v_{\text{esc}}), \quad (2.1)$$

where  $\mu_{\chi p}^2$  is the reduced mass of the WIMP-nucleon system,  $A$  is the atomic mass number of the target nucleus,  $F_N^2(E_R)$  is the nuclear form factor of the target nucleus, and  $\mathcal{G}(v_{\text{min}}, v_{\text{esc}})$  parametrizes the DM velocity distribution in the halo. Here we consider it as given by an integration of a Maxwell-Boltzmann distribution,  $f(\mathbf{v}, v_0)$ , and neglect the uncertainties associated with deviating from it [70–72],

$$\mathcal{G}(v_{\text{min}}, v_{\text{esc}}) = \rho_0 \int_{v_{\text{min}} < |\mathbf{v}| < v_{\text{esc}}} \frac{f(\mathbf{v}, v_0)}{|\mathbf{v}|} d^3v. \quad (2.2)$$

The “minimal” velocity,  $v_{\text{min}}$ , also depends on the recoil energy  $E_R$  and atomic mass of the target  $m_N$ ,<sup>2</sup>

$$v_{\text{min}} = \frac{1}{\sqrt{2E_R m_N}} \left( \frac{E_R m_N}{\mu_{\chi N}} \right). \quad (2.3)$$

Because the experiments are in general well shielded by construction, and the purity of the target material is very high, we neglect in this paper a very small residual background which is usually further reduced by applying one or another discrimination method. The effect of the residual backgrounds on WIMP property reconstruction has been considered in the literature [16, 18]. Note that we also neglect in this paper the limitation arising from the statistical scattering of the measured event around the real  $dR/dE_R$  [73].

One can obtain information on the input parameters  $\{p\}_{\text{DD}}$  by confronting the expected signal times exposure to the (mock) measured signal. This is done here through a binned likelihood function that is a product of Poisson distributions independently evaluated in  $i = 1, \dots, N_{\text{DD}}$  energy bins equally spaced in logarithmic intervals. We choose here logarithmic intervals to overcome possible bias towards the low recoil-energy bins. This can occur when the signal is not very strong, as the tail of the event distribution becomes indistinguishable from zero in the bins above a certain cutoff energy, which does not in general coincide with the nominal cutoff energy of the experiment.

In each bin the measured number of events,  $n_i$ , is compared to the calculated signal,  $\mu_i(\{p\}_{\text{DD}})$ , given by

$$\mu_i = \text{exposure} \times \int_{E_{R,i-1}}^{E_{R,i}} \frac{dR}{dE_R} dE_R. \quad (2.4)$$

The likelihood function reads

$$\mathcal{L}_{\text{DD}} = \prod_{i=1}^{N_{\text{DD}}} \frac{\mu_i^{n_i} e^{-\mu_i}}{n_i!}. \quad (2.5)$$

## 2.2 Gamma-ray signals from dwarf spheroidal galaxies and the Galactic Center

We will now consider a WIMP discovery in gamma-ray observatories. Because of their highly reduced backgrounds, the targets most sensitive to observation of DM in the 10 – 250 GeV range are the dSphs from the Local Group. To analyze a realistic scenario we consider here the sensitivity obtained with 15 years data, from observation of 46 dSphs. We mimic 46 dSphs by modeling the

---

<sup>2</sup>We assume here elastic scattering of DM particles off nuclei (for a discussion of inelastic scattering see, e.g., [21] and references therein).

signal in the presently discovered 23 dSphs, and successively doubling it. Conversely, for DM masses above 250 GeV the highest sensitivity is expected at CTA in observation of the GC.

The expected differential flux from WIMP annihilation depends on the input parameters  $\{p\}_{\gamma\text{-rays}} = \{m_\chi, \sigma v, f\}$ , where  $f$  parametrizes a set of branching ratios to different annihilation final states. In the case of one dSphs, the observed flux reads

$$\left(\frac{d\Phi}{dE}\right)_{\text{dSphs}} = \frac{\sigma v}{8\pi m_\chi^2} J \frac{dN_\gamma}{dE}, \quad (2.6)$$

where  $J$  is the  $J$ -factor measured for all dSphs from velocity dispersion relations [74–77] and  $dN_\gamma/dE$  is the prompt gamma-ray spectrum from WIMP annihilation, which depends on the annihilation final state.

In the case of observation of the GC, one must additionally factor in the large uncertainties of the halo profile determinations. We do so by assuming a generalized Navarro-Frenk-White (NFW) profile [64]

$$\rho(r) = \frac{\rho_0 \left(1 + \frac{R_\odot}{r_s}\right)^{3-\gamma_{\text{NFW}}}}{\left(\frac{r}{R_\odot}\right)^{\gamma_{\text{NFW}}} \left(1 + \frac{r}{r_s}\right)^{3-\gamma_{\text{NFW}}}} \quad (2.7)$$

where we fix the scale radius  $r_s = 20$  kpc and the distance of the Solar System from the GC,  $R_\odot = 8.5$  kpc. This introduces two new free input parameters to our analysis:  $\{p\}_{\gamma\text{-rays}} = \{m_\chi, \sigma v, f, \rho_0, \gamma_{\text{NFW}}\}$ . The  $J$ -factor for a region of the GC characterized by a solid angle  $\Delta\Omega$  is given by integrating  $\rho^2(r)$  along the line of sight in the corresponding angular region,

$$J_{\Delta\Omega} = \int_{\Delta\Omega} \int_{\text{l.o.s.}} \rho^2[r(\theta)] dr(\theta) d\Omega. \quad (2.8)$$

A calculation of the flux from the GC must take into account the prompt spectrum and the secondary spectrum from inverse Compton (IC) scattering of electrons off the CMB, starlight, and IR radiation [48, 78], so that one gets

$$\left(\frac{d\Phi}{dE}\right)_{\text{GC}} = \frac{\sigma v}{8\pi m_\chi^2} \left( J_{\Delta\Omega} \frac{dN_\gamma}{dE} + \frac{1}{E^2} \int_{m_e}^{m_\chi} dE_s \bar{I}_{\text{IC},\Delta\Omega}(E, E_s) \frac{dN_{e^\pm}}{dE_s} \right), \quad (2.9)$$

where  $dN_{e^\pm}/dE$  stands for the electron/positron spectra from WIMP annihilation. The quantity  $\bar{I}_{\text{IC},\Delta\Omega}$  parametrizes the cumulative effect of the differential IC radiation power per unit of Galactic coordinates [78], which we here call  $I_{\text{IC}}(E_\gamma, E_s, l, b)$ . It is explicitly given by

$$\bar{I}_{\text{IC},\Delta\Omega}(E_\gamma, E_s) = 4R_\odot \rho_0^2 \int_{\Delta l, \Delta b} I_{\text{IC}}(E_\gamma, E_s, l, b) dl db \cos b, \quad (2.10)$$

where  $R_\odot$  is the distance of the Sun from the GC and we use for the computation the form of  $I_{\text{IC}}(E_\gamma, E_s, l, b)$  provided by [78].

### 2.2.1 Likelihood function for Fermi-LAT dSphs

We consider a binned likelihood function for the putative data in 46 dSphs at Fermi-LAT.

The gamma-ray flux, Eq. (2.6), is binned into  $N_{\text{Fermi}} = 17$  energy bins and then confronted to the putative observed residual flux. Each different dwarf galaxy is labeled by the index  $j = 1, \dots, 46$  so that the expected flux in each bin is given by  $\frac{d\Phi_j}{dE_i} \equiv \frac{d\Phi_j}{dE}(E_i)$ .

For each dSphs the corresponding  $J$ -factor,  $\bar{J}_j$ , has been computed by the Fermi-LAT Collaboration with a relative logarithmic uncertainty,  $\sigma_j$  [77]. The expected flux is compared to the mock observed flux in bin  $ij$ ,  $\frac{d\Phi_j}{dE_i}$ , through the likelihood function

$$\mathcal{L}_{\text{dSphs}} = \prod_{j=1}^{46} \left\{ \int \frac{dJ_j}{\log(10)\bar{J}_j\sqrt{2\pi}\sigma_j} \exp \left[ -\frac{(\log_{10} J_j - \log_{10} \bar{J}_j)^2}{2\sigma_j^2} \right] \times \right. \\ \left. \times \prod_{i=1}^{N_{\text{Fermi}}} \frac{1}{\sqrt{2\pi}\bar{\sigma}_{ij}} \exp \left[ -\frac{\left( \frac{d\Phi_j}{dE_i} - \frac{d\bar{\Phi}_j}{dE_i} \right)^2}{2\bar{\sigma}_{ij}^2} \right] \right\}. \quad (2.11)$$

The uncertainties  $\bar{\sigma}_{ij}$  are estimated by generating the total expected flux from the signal, as well as the isotropic and diffuse background [79] for each dwarf galaxy. This is translated into the total number of expected events for the observation period by convolving with the exposure map and observation time [80]. The uncertainty in the total number of gamma rays in a given observation region and energy bin is then taken as the Poisson uncertainty. The error in the residual flux is calculated as the uncertainty in the total number of gamma rays converted back into a flux by dividing by the exposure. Note that the uncertainties  $\bar{\sigma}_{ij}$  are thus related to the backgrounds in each dwarf galaxy and each energy bin and therefore also depend on  $J_j$ .

### 2.2.2 Likelihood function for CTA

To construct the likelihood function for CTA we use a generalization of the *Ring Method* based on four spatial regions or patches in sky.<sup>3</sup> The four regions we consider are identified in the plane of the Galactic angular coordinates  $l$  and  $b$ , as shown in Fig. 1. Region 1, in which DM annihilations are likely to play a more important role than in other places in the sky, is defined as a circle of angular radius  $\Delta_1 = 1.0^\circ$  around the GC. Region 2 covers the angular corona included between  $\Delta_1$  and  $\Delta_2 = 1.36^\circ$ . In addition we define two regions (Regions 3 and 4) where the expected count has only a minor contribution from the DM signal. Regions 3 and 4 are respectively included in the lower and upper halves of a ring centred at the offset coordinate  $b_{\text{off}} = 1.42^\circ$ . The inner angular region of radius  $r_1 = 0.55^\circ$  is not considered, whereas the outer radius of the ring including Regions 3 and 4 is  $r_2 = 2.88^\circ$ . Regions 1, 2, and 3 belong to the lower half of the ring of outer radius  $r_2$  without overlapping. The strip of sky characterised by  $|b| < 0.3^\circ$  about the Galactic plane does not belong to any of the considered regions.

We bin the  $\gamma$ -ray spectra into  $N_{\text{CTA}} = 30$  energy bins,  $i = 1, \dots, N_{\text{CTA}}$ , logarithmically spaced. Regions 1 to 4 are labeled with an index  $j$ . For each bin,  $ij$ , the signal is assumed to be composed of three parts: the DM signal,  $\mu_{ij}^{\text{DM}}$ , which originates from WIMP annihilations in the halo; the isotropic background  $\mu_{ij}^{\text{CR}}$  from cosmic-ray (CR) showers, which is obtained by detailed MC simulation and was provided to us by the CTA Collaboration [81]; and the Galactic Diffuse Emission (GDE) background [80, 82, 83],  $\mu_{ij}^{\text{GDE}}$ , which is obtained from Fermi-LAT data for the energy bins below 500 GeV, and extrapolated with a power law for higher energies, as described, e.g., in [46, 48].

Explicitly, this reads

$$\mu_{ij}^{\text{DM}} = t_{\text{obs}} \int_{\Delta E_i} dE \frac{1}{\sqrt{2\pi}\delta(E)^2} \int_{30 \text{ GeV}}^{m_\chi} dE' \left( \frac{d\Phi_j}{dE'} \right)_{\text{GC}} A_{\text{eff}}(E') e^{-\frac{(E-E')^2}{2\delta(E)^2}}, \quad (2.12)$$

<sup>3</sup>The Ring Method is generally based on two spatial regions [43–46]. We will show in Sec. 4 that, by adding one region to the traditional two, one improves significantly the background reduction, and the results do not then improve as much by adding additional patches.

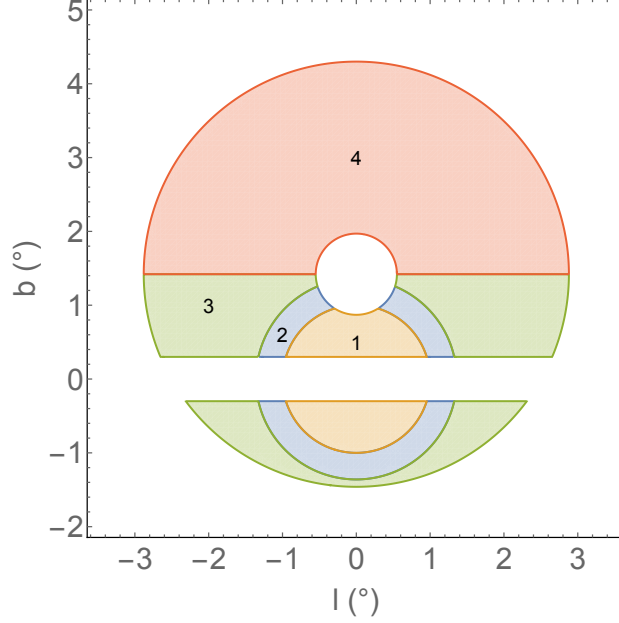


**Figure 1:** Our generalization of the Ring Method. Region 1 (beige), is inside the circle of angular radius  $\Delta \leq 1.0^\circ$ . Region 2 (light blue) is the angular corona included in  $1.00^\circ < \Delta \leq 1.36^\circ$ . Region 3 is marked with light green and Region 4 with salmon pink. The ring's center is offset from the GC by  $b_{\text{off}} = 1.42^\circ$ . Its inner radius is  $r_1 = 0.55^\circ$  and its outer radius is  $r_2 = 2.88^\circ$ . The strip of the sky at  $|b| < 0.3^\circ$  (Galactic plane) does not belong to any of the regions.

where  $A_{\text{eff}}$  is the effective area of the detector,  $\delta(E)$  is the energy resolution, and  $(d\Phi_j/dE)_{\text{GC}}$  is the gamma-ray flux from WIMP annihilation in the  $j$ th region of the sky, defined in Eq. (2.9). For  $A_{\text{eff}}$  and  $\delta(E)$  we use recent instrument response functions provided by the CTA Collaboration [81]. The  $J$ -factors,  $J_j$ , are calculated over each region of the sky.

In order to obtain the total count number per bin  $\mu_{ij}$ , which is to be confronted with our putative signal,  $n_{ij}$ , the backgrounds must be added to the DM signal,

$$\mu_{ij}(R_i^{\text{CR}}, R_i^{\text{GDE}}) = \mu_{ij}^{\text{DM}} + R_i^{\text{CR}} \mu_{ij}^{\text{CR}} + R_i^{\text{GDE}} \mu_{ij}^{\text{GDE}}, \quad (2.13)$$

where we parametrize the uncertainty in the normalization of the CR and GDE backgrounds with additional energy bin-dependent factors  $R_i^{\text{CR}}$  and  $R_i^{\text{GDE}}$ . Throughout the paper we assume that the measured value of the total CR flux and of the GDE at energies  $< 500 \text{ GeV}$  indirectly imply that  $R_i^{\text{CR}}$  and  $R_i^{\text{GDE}}$  are normally distributed around 1. We adopt conservative uncertainties  $\sigma_{\text{CR}} = 10\%$  and  $\sigma_{\text{GDE}} = 20\%$ . The CTA likelihood function is thus given by

$$\mathcal{L}_{\text{CTA}} = \prod_{i=1}^{N_{\text{CTA}}} \left\{ \int dR_i^{\text{CR}} e^{-\frac{(1-R_i^{\text{CR}})^2}{2\sigma_{\text{CR}}^2}} \int dR_i^{\text{GDE}} e^{-\frac{(1-R_i^{\text{GDE}})^2}{2\sigma_{\text{GDE}}^2}} \times \left[ \prod_{j=1}^4 \frac{\mu_{ij}(R_i^{\text{CR}}, R_i^{\text{GDE}})^{n_{ij}}}{n_{ij}!} e^{-\mu_{ij}(R_i^{\text{CR}}, R_i^{\text{GDE}})} \right] \right\}. \quad (2.14)$$

Note that, neglecting for a moment the spread in  $\rho_0$  and  $\gamma_{\text{NFW}}$ , a minimum number of three regions in the sky is necessary to constrain independently the three quantities at the origin of the

	BP1	BP2	BP3	BP4(a, b, c, d)	BP5
$m_\chi$	25 GeV	100 GeV	250 GeV	1000 GeV	1000 GeV
$\sigma v$	$8 \times 10^{-27} \text{ cm}^3/\text{s}$	$2 \times 10^{-26} \text{ cm}^3/\text{s}$	$4 \times 10^{-26} \text{ cm}^3/\text{s}$	$2 \times 10^{-25} \text{ cm}^3/\text{s}$	$3 \times 10^{-26} \text{ cm}^3/\text{s}$
$\sigma_p^{\text{SI}}$	$2 \times 10^{-46} \text{ cm}^2$	$3 \times 10^{-46} \text{ cm}^2$	$5 \times 10^{-46} \text{ cm}^2$	$2 \times 10^{-45} \text{ cm}^2$	$2 \times 10^{-45} \text{ cm}^2$
Final state (hadronic scans)	$b\bar{b}$	$b\bar{b}$	$b\bar{b}$	(a) $b\bar{b}$ (b) $W^+W^-$ (c) $\tau^+\tau^-$	$W^+W^-$
Final state (leptonic scan)				(d) $\mu^+\mu^-$	

**Table 1:** Parameters of the 8 benchmark points that ought to be reconstructed through our scanning procedure. In “hadronic” scans we allow for 4 final-state channels such that the branching fractions sum up to 1:  $f_{b\bar{b}} + f_{W^+W^-} + f_{hh} + f_{\tau^+\tau^-} = 1$ . In the “leptonic” scan we allow for 3 final-state channels:  $f_{b\bar{b}} + f_{\mu^+\mu^-} + f_{\tau^+\tau^-} = 1$ .

flux normalization:  $\sigma v$ ,  $R_i^{\text{CR}}$ , and  $R_i^{\text{GDE}}$ . It has been previously shown in the literature [46] that, when deriving CTA upper bounds on the DM annihilation cross section, a morphological analysis that divides the sky in several regions leads to a significant increase in sensitivity with respect to the traditional Ring Method. We will see in Sec. 4 that for reconstructing the DM properties the greatest improvement is obtained by extending the Ring Method by one region, even in the case where  $\rho_0$  and  $\gamma_{\text{NFW}}$  are treated as nuisance parameters, and that adding even more patches introduces a more moderate, incremental improvement.

Finally, note that we do not include in this study systematic uncertainties in the CTA detector response [46], which are to some extent unknown at this point, and further systematic effects that can be present such as varying acceptance across the field of view or uncertainties in the effective area.

### 3 Benchmark points and scanning methodology

We engineer eight benchmark points to generate mock signals in the experiments described in Sec. 2. The benchmark point parameters are summarized in Table 1.

We re-emphasize that our benchmark points do not assume any particular particle theory model. We thus treat  $\sigma_p^{\text{SI}}$ ,  $\sigma v$ , and the final state branching ratios as independent parameters that are only constrained by experiments. Nor do we impose the relic density constrain. Note that although in several models  $\sigma_p^{\text{SI}}$  and  $\sigma v$  can feature some degree of correlation, this is not always warranted. For example, in the familiar case of the MSSM  $\sigma_p^{\text{SI}}$  and  $\sigma v$  do not show correlation in global analyses (see, e.g., [47]).

Given four benchmark masses selected across the WIMP mass range typically considered in the literature ( $m_\chi = 25, 100, 250, 1000 \text{ GeV}$ ), we choose the benchmark values of  $\sigma_p^{\text{SI}}$  and  $\sigma v$  such that they can lead to a strong signal in either direct or indirect detection experiments, or both, given realistic expectations for the projected future sensitivity. At the same time, we make sure these points are not excluded by the current experimental bounds. In particular, we choose  $\sigma v$  to lie on the published 95% C.L. exclusion line of the most recent analysis that combines the 6 year PASS 8 data for 15 dSphs at Fermi-LAT with observations from the GC at MAGIC [84].

Here we briefly comment on our benchmark points.

- **BP1:** This is the case of a relatively light WIMP,  $m_\chi = 25 \text{ GeV}$ , annihilating exclusively (100% branching ratio) into hadronic products ( $b\bar{b}$  final state). The strongest sensitivity to  $\sigma_p^{\text{SI}}$  in Xenon underground detectors is achieved approximately at this mass, and the current direct detection bound is  $\sigma_p^{\text{SI}} \lesssim 10^{-45} \text{ cm}^2$ .

	Acceptance	Recoil energy range	Exposure
XENON-1T (Xe)	40%	4 – 50 keV	730 ton days (all BPs)
SCDMS-Snolab (Ge)	50%	8 – 115 keV	1150 ton days (BP1) 1100 ton days (BP2) 950 ton days (BP3) 900 ton days (BP4)
DarkSide-G2 (Ar)	Ref. [68]	38 – 200 keV	– (BP1) 7300 ton days (BP2) 4300 ton days (BP3) 3300 ton days (BP4)

**Table 2:** The experiments for which we consider a putative signal in direct detection. Exposure has been adjusted in Ge and Ar experiments to reach a sensitivity to the benchmark points equal to the one in XENON-1T with 730 ton days. For DarkSide-G2 we consider a recoil-energy dependent acceptance, see Fig. 6 in Ref. [68].

- **BP2:** A benchmark characterized by  $m_\chi = 100$  GeV, possibly motivated by models with rough expectations of EW naturalness. The sensitivity of direct detection experiments currently implies  $\sigma_p^{\text{SI}} \lesssim 2 \times 10^{-45} \text{ cm}^2$ . The annihilation final state is set to 100%  $b\bar{b}$ .
- **BP3:** A benchmark characterized by  $m_\chi = 250$  GeV, situated at the possible onset of the Fermi-LAT/CTA interplay for mass and final state reconstruction. The annihilation final state is set to 100%  $b\bar{b}$ .
- **BP4(a):** As was mentioned in Sec. 1, a  $\sim 1$  TeV WIMP is characteristic of many GUT-constrained models based on supersymmetry with neutralino DM.

Even if we do not make any assumptions on the relic density, it is worth pointing out that the Fermi-LAT/MAGIC bound [84] for an  $m_\chi = 1000$  GeV WIMP with 100%  $b\bar{b}$  final state reads  $\sigma v = 2 \times 10^{-25} \text{ cm}^3/\text{s}$ . This is a value that is larger than the cross section expected for a “canonical” thermal candidate. However, it is well known that the present-day annihilation cross section does not need to coincide with the thermal annihilation cross section in the early Universe. Examples can be easily found in which the WIMP has the correct relic abundance but the present-day annihilation cross section is slightly enhanced, for example by an  $s$ -channel resonance with the exchange of a particle with mass  $\approx 2m_\chi = 2$  TeV (in the case of supersymmetry this particle is often the pseudoscalar Higgs).

- **BP4(b, c, d):** We investigate the ability of CTA to reconstruct annihilation final states different from pure  $b\bar{b}$  for the same  $\sigma v$ .
- **BP5:** We also consider the case of a 1 TeV WIMP with the canonical thermal  $\sigma v \approx 3 \times 10^{-26} \text{ cm}^3/\text{s}$  and 100% branching ratio to  $W^+W^-$  (typical, again, of some popular supersymmetric candidates but present also in other models [85]).

For each of the benchmark points we perform a global scan of the parameter space, where the scans are guided by a global likelihood function that includes the different pieces described in Sec. 2. To each piece there corresponds a different experiment: three direct detection experiments and two gamma-ray telescopes. To make contact with current and realistic or planned experiments we indicatively select XENON-1T [28] for a Xe target, SuperCDMS-Snolab [86, 87] for a Ge target, and for Ar the planned experiment DarkSide-G2 [42]. The schematic characteristics of the three experiments considered here are given in Table 2. In this paper we use units of ton days to quantify



Symbol	Parameter	Scan range	Prior distribution
$m_\chi$	WIMP mass	10 – 10000 GeV	log
$\sigma v$	Annihilation cross section	$10^{-30} - 10^{-21} \text{ cm}^3/\text{s}$	log
$\sigma_p^{\text{SI}}$	Spin-independent cross section	$10^{-48} - 10^{-42} \text{ cm}^2$	log
<i>Hadronic benchmark points</i>			
$f_{b\bar{b}}$	Branching ratio $b\bar{b}$ final state	0 – 1*	See text
$f_{WW}$	Branching ratio $WW$ final state	0 – 1	See text
$f_{hh}$	Branching ratio $hh$ final state	0 – 1	See text
$f_{\tau\tau}$	Branching ratio $\tau\tau$ final state	0 – 1	See text
<i>Leptonic benchmark point –BP4(d)</i>			
$f_{\text{lep}}$	Branching ratio leptons	0 – 1*	See text
$f_{\text{had}}$	Branching ratio hadrons	0 – 1	See text
$f_{\tau\tau}$	Branching ratio $\tau\tau$ final state	0 – 1	See text
<i>Nuisance parameters</i>			
$v_0$	Circular velocity	$220 \pm 20 \text{ km/s}$	Gaussian
$v_{\text{esc}}$	Escape velocity	$544 \pm 40 \text{ km/s}$	Gaussian
$\rho_0$	Local DM density	$0.3 \pm 0.1 \text{ GeV/cm}^3$	Gaussian
$\gamma_{\text{NFW}}$	NFW slope parameter	$1.20 \pm 0.15$	Gaussian

\*The sum of the branching ratios is 1 and the prior is a modified Dirichlet distribution (see text).

**Table 3:** Input parameters in our scans.

exposure in direct detection experiments. Note that the exposure has been adjusted in Ge and Ar experiments to reach the sensitivity to the signal generated by the benchmark points equal to the one in XENON-1T with  $\sim 2$  years of data. Note that for DarkSide-G2 we consider a recoil-energy dependent acceptance, which we borrow from Fig. 6 of Ref. [68]. For indirect detection, we consider signals at Fermi-LAT and CTA, as described in Sec. 2. We consider a default target observation time of 500 hours for CTA and 15 years 46 dSphs in Fermi-LAT.

The scanning sampling is performed with `MultiNest` [88]. Recoil energy rates  $dR/dE_R$  are computed with `micrOMEGAs v.4.1.5` [89], while annihilation spectra for gamma-ray fluxes,  $d\Phi/dE$ , are obtained using [78, 90, 91]. The uncertainties in Fermi-LAT are calculated as described in Sec. 2.2.1 with the help of the Fermi Science Tools [80]. The scanned input parameters, their ranges, and their prior distributions are given in Table 3. The nuisance parameters are fixed at their central values in the benchmark points.

In each scan the global likelihood function is given by the product of Eqs. (2.5), (2.11), (2.14), and the Gaussian likelihood functions associated with the nuisance parameters (see Table 3). A global test statistics is then constructed according to the profile likelihood technique. We remind the reader that inference on a subset of  $r \leq n$  specific model parameters or observables, or a combination of both (collectively denoted by  $\psi_i$ ) is drawn by “profiling” the global likelihood function along the other directions in the parameter space,

$$\mathcal{L}(\psi_{i=1,\dots,r}) = \max_{\psi_i \in \mathbb{R}^{n-r}} \mathcal{L}(\psi_{i=1,\dots,n}). \quad (3.1)$$

Confidence intervals are calculated from tabulated values of  $\Delta\chi^2 \equiv -2\ln(\mathcal{L}/\mathcal{L}_{\text{max}})$ . For example, in  $r = 2$  dimensions, 95.0% confidence regions are given by  $\Delta\chi^2 = 5.99$ .

In the case of BP4, to which CTA shows the highest sensitivity, we run two different types of scans. “Hadronic” scan inputs (for fitting to BP4(a)-(c)) use a combination of 4 types of hadronic spectra, which present similar shapes and normalizations:  $b\bar{b}$ ,  $W^+W^-$ ,  $hh$ , and  $\tau^+\tau^-$ . In the “leptonic” scan (BP4(d)) we investigate whether distinguishing between hadronic and leptonic spectra is

easier than distinguishing among 4 different hadronic spectra. We thus consider 3 final-state input channels:  $b\bar{b}$ ,  $\mu^+\mu^-$ , and  $\tau^+\tau^-$ .

In order to avoid introducing statistical bias towards points characterized by pure final states or, alternatively, by maximal admixtures of different final states, which would create unphysical inhomogeneities in the density of points appearing in the plots, we modify a prior Dirichlet distribution for the branching ratios so that eventually all marginal one-dimensional distributions for the individual branching ratios are close to being uniform. We remind the reader that from a frequentist point of view the priors should not matter in the results, so that this choice is merely driven by aesthetic reasons.

It is also possible to study model-dependent priors that introduce specific fixed relations between different branching ratios, e.g., between  $\mu^+\mu^-$  and  $e^+e^-$  or between  $W^+W^-$  and  $hh$ , for priors motivated by Minimal Flavor Violation or by gauge symmetry, respectively. By effectivelly being equivalent to a redefinition of the number of independent parameters, this could eventually affect the DM reconstruction. We will not investigate this issue in more detail in the present paper.

## 4 Discussion of results

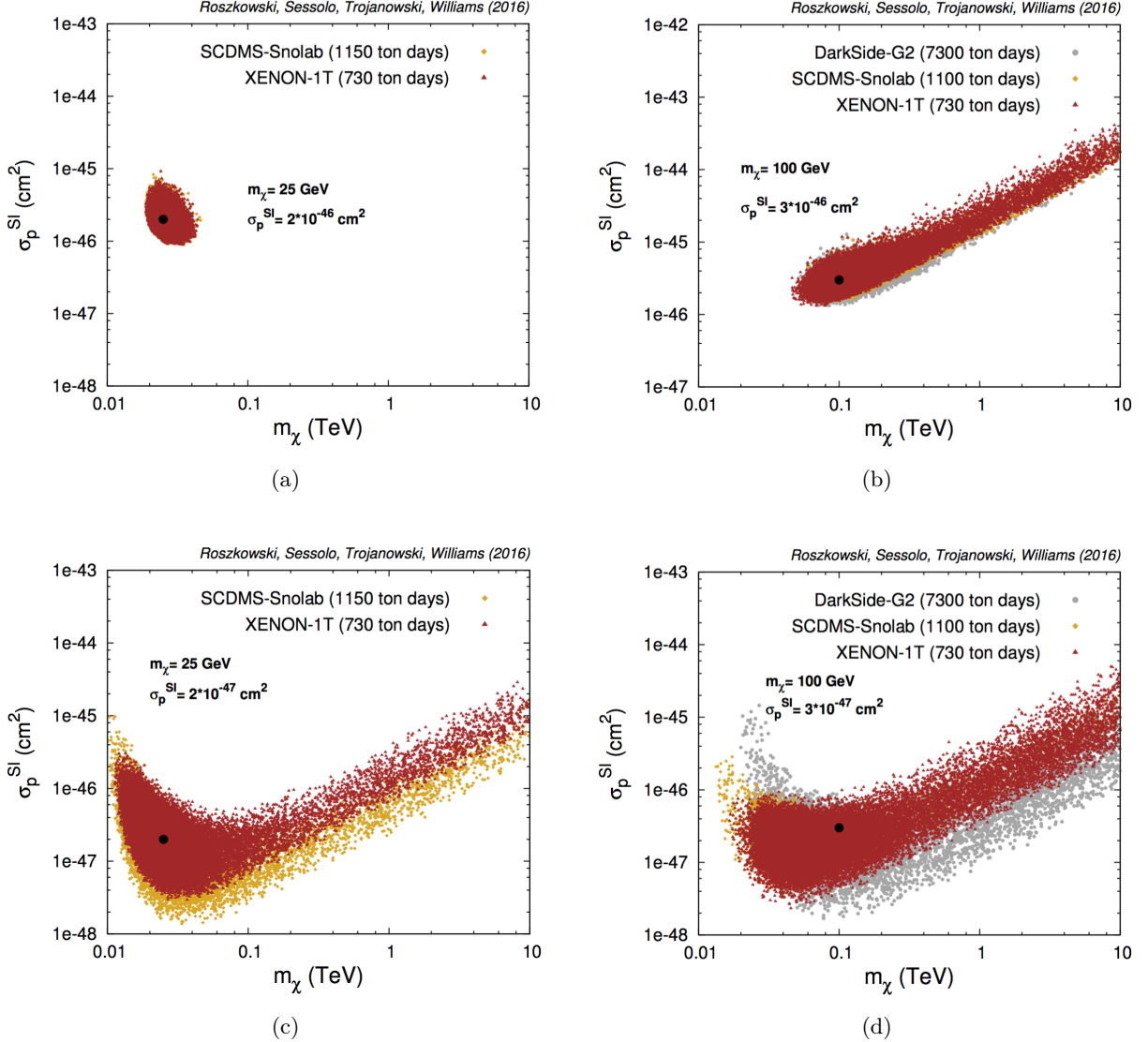
We present here the results of fitting the mock data with the likelihood functions defined in Secs. 2 and 3. In all the plots we show points that are consistent at the 95% C.L. with the mock data in different experiments and with the current measurements of the nuisance parameters.

To make contact with the existing literature, we first re-derive the case of direct detection, which has been extensively discussed [12–22]. As was mentioned in Sec. 2, for a given exposure direct detection experiments based on different target materials and/or characterized by different detector acceptances will not reach the same sensitivity. We showed in Table 2 that, if one assumes that a WIMP discovery will be made in a Xenon detector of  $\sim 1$  ton fiducial mass with 2 years of data, it will in general take a longer time or a greater mass to reach the same sensitivity in detectors based on Ge or Ar. Experiments based on Argon, in particular, need large exposures.

On the other hand, the relative importance of the current astrophysical uncertainties for the inability to fully reconstruct WIMP mass or cross section in one or another direct detection experiment can only be gauged properly when all experiments reach comparable sensitivity. We thus make this assumption in what follows. Note that for BP1 in Table 1, characterized by  $m_\chi = 25$  GeV, the required exposure in an Argon experiment to be competitive with detectors based on Xe or Ge becomes much greater than 20 ton years, and for this reason we do not try to reconstruct BP1 in an Ar experiment.

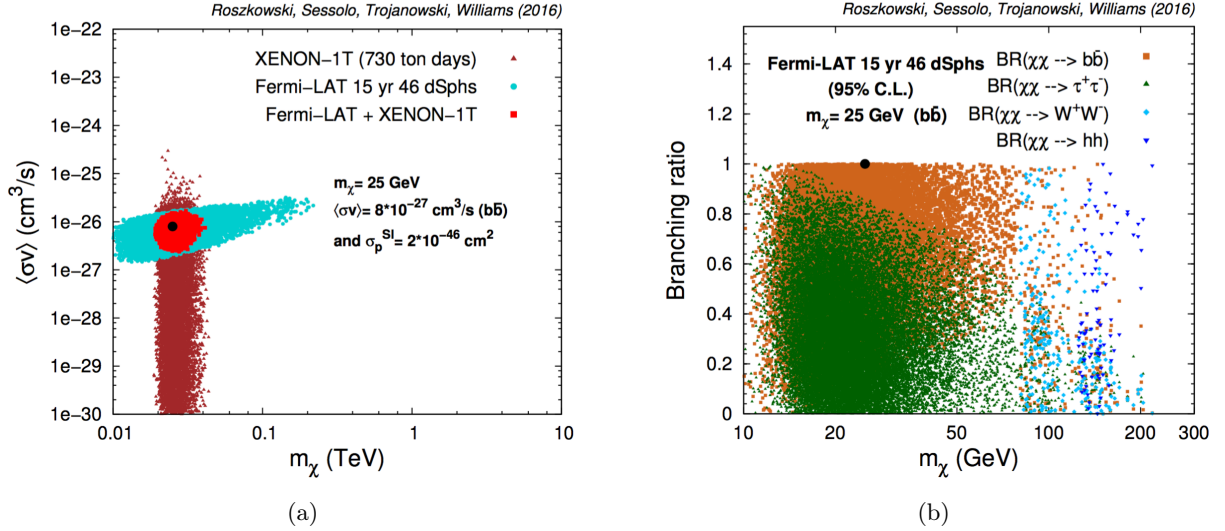
In Fig. 2(a) we show the 95% C.L. reconstruction of BP1 in the  $(m_\chi, \sigma_p^{\text{SI}})$  plane. We take XENON-1T as a representative of a Xe experiment and SuperCDMS-Snolab as a proxy for a Ge experiment. The 95% C.L. regions, shown with brown triangles for Xenon and golden-rod diamonds for Germanium, overlap when the experiments reach the same sensitivity. The WIMP mass and scattering cross section can be reconstructed to good precision, in agreement with what has been shown in the literature (see, e.g., [22]). The residual uncertainties of the mass amount to approximately a factor 2 and of the cross section to approximately one order of magnitude. They are due to the uncertainties in the nuisance parameters  $\rho_0$ ,  $v_0$ , and  $v_{\text{esc}}$ .

Good reconstruction for WIMP mass and cross section in direct detection is expected as long as the WIMP mass is not much larger than the mass of the nuclei of the target material. The experiments lose sensitivity, irrespective of the target material, when  $m_\chi$  becomes greater or equal to approximately 100 GeV. This is shown in Fig. 2(b), where we present the 95% C.L. reconstruction of point BP2, characterized by  $m_\chi = 100$  GeV. Note that we add an Argon experiment to the lot (dark gray circles), which we model after DarkSide-G2, and which requires an exposure 10



**Figure 2:** (a) Brown triangles show the 95% C.L. fit in the  $(m_\chi, \sigma_p^{\text{SI}})$  plane to BP1 data in a Xenon experiment (XENON-1T) with 730 ton days exposure (the benchmark is shown in black). The same sensitivity can be reached in a Germanium experiment (SuperCDMS-Snolab) with approximately 1150 ton days. The corresponding 95% C.L. region is shown with golden-rod diamonds. (b) The 95% C.L. region fit (brown triangles) to BP2 data in XENON-1T. Fit to data in SuperCDMS-Snolab is shown with golden-rod diamonds, and the 95% C.L. region in DarkSide-G2, as a proxy for a generic Argon experiment, is shown with dark gray circles. (c) The 95% C.L. region fit to a point characterized by  $\sigma_p^{\text{SI}}$  lower than in BP1 by one order of magnitude. The color code is the same as in (a). (d) The 95% C.L. region fit to a point characterized by  $\sigma_p^{\text{SI}}$  lower than in BP2 by one order of magnitude. The color code is the same as in (b).

times as large as XENON-1T to reach a comparable sensitivity. However, again one can see that equivalent sensitivities produce equivalent regions in the  $(m_\chi, \sigma_p^{\text{SI}})$  plane. We neglect to show here the reconstructions of the heavier benchmark points, BP3 (250 GeV) and BP4 (1000 GeV) in



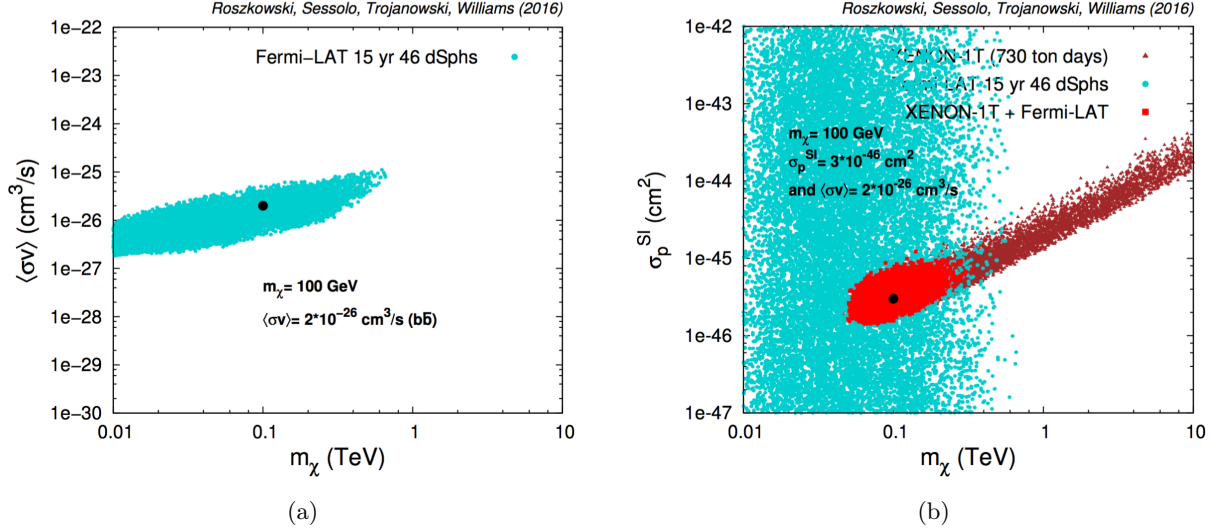
**Figure 3:** (a) Dark turquoise circles show the 95% C.L. fit to Fermi-LAT 15 yr 46 dSphs mock BP1 data in the  $(m_\chi, \sigma v)$  plane (the benchmark point is shown in black). Brown triangles show the fit to the corresponding XENON-1T data with 730 ton days exposure. The 95% C.L. combination of the two experiments in the  $(m_\chi, \sigma v)$  plane is shown with red squares. (b) The breakdown of the branching ratios to a particular annihilation final state versus the WIMP mass for the points of the 95% C.L. fit to Fermi-LAT data considered in (a). Light brown squares show the  $b\bar{b}$  branching ratio, dark green triangles the one to  $\tau^+\tau^-$ , deep-sky blue diamonds the one to  $W^+W^-$ , and blue upside-down triangles the one to  $hh$ .

Table 1, as the confidence regions look like in Fig. 2(b) despite the points being further up the reconstructed band.

We remind the reader here that, because of the near absence of background, the reconstruction quality is strongly affected by the Poisson uncertainties so that increasing exposure plays a pivotal role in improving the quality of reconstruction. In this regard, one can see in Figs 2(c) and 2(d), where we show the 95% C.L. regions for points featuring  $\sigma_p^{\text{SI}}$  exactly one order of magnitude lower than in BP1 and BP2, that, given the designed exposures, the experiments lose much if not all of their reconstruction power, even when  $m_\chi = 25$  GeV.

As reconstructing the properties of the DM particle in direct detection becomes difficult for WIMPs characterized by mass around and above the electroweak scale, we here proceed to investigate how an indirect detection in one or more of the gamma-ray observatories introduced in Sec. 2 can provide enough information to derive the WIMP properties, or at least improve over a detection in underground laboratories. While there is no doubt that a real signal should be detected in all the experiments that are sensitive to the same observables, one can find several models of DM that are likely to produce a strong signal only in direct or indirect detection. For this reason, although the main purpose of this paper is to investigate the interplay of different experimental strategies in case of concurrent detection, it is also important to quantify how well information can be reconstructed in each experiment separately.

In Fig. 3(a) we show with dark turquoise circles the 95% C.L. region for Fermi-LAT 15 yr 46 dSphs in the  $(m_\chi, \sigma v)$  plane for BP1. The cross section spread due to the uncertainties described in Sec. 2.2.1 is about one order of magnitude, whereas the derived uncertainty of the mass



**Figure 4:** (a) The 95% C.L. fit to Fermi-LAT 15 yr 46 dSphs mock BP2 data in the  $(m_\chi, \sigma v)$  plane (the benchmark point is shown in black). (b) The 95% C.L. region fit to BP2 data in XENON-1T in the  $(m_\chi, \sigma_p^{SI})$  plane is shown with brown triangles. Dark turquoise circles show the 95% C.L. fit to Fermi-LAT 15 yr 46 dSphs data. The 95% C.L. combination of the two experiments in the  $(m_\chi, \sigma_p^{SI})$  plane is shown with red squares.

reconstruction is much larger. Note that CTA is not sensitive to a light WIMP signal from the GC, so that it cannot help improve on the poor mass reconstruction. Given realistic expectations for the experiments of the near future little more can be said in gamma-ray experiments for this benchmark point. Possibly the next generation of anti-proton observatories will be able to provide some complementarity but this is beyond the scope of this paper.

The mass degeneracy observed in the fit to gamma-ray data is associated with a degeneracy in the possible final state products (we remind the reader that for BP1 we fit to 4 possible final states, all yielding in some large percentage to hadrons, see Sec. 3). The benchmark BP1 is characterized by 100%  $b\bar{b}$  branching ratio. However, Fig. 3(b) shows that the Fermi-LAT mock data can be fitted to the same precision by tau-dominated cases with  $m_\chi \approx 10 - 15$  GeV (dark green triangles), or by cases with  $m_\chi \gtrsim 100$  GeV and admixtures of  $b\bar{b}$  (light brown squares) and  $W^+W^-$  (deep-sky blue diamonds) or  $hh$  (dark blue down-pointing triangles). We will come back to discussing the degeneracy due to different final states below.

On the other hand, for large enough  $\sigma_p^{SI}$  as to allow for concurrent signatures in direct and indirect detection the complementarity of these two venues can be used to narrow down the mass and annihilation final state. In Fig. 3(a) we project the 95% C.L. region for XENON-1T (brown triangles) into the  $(m_\chi, \sigma v)$  plane. The 95% C.L. combined region for Fermi-LAT and XENON-1T is then shown with red squares. Intersecting the two regions allows one to strongly narrow down the uncertainties of the mass determination.

Note that if one restricts Fig. 3(b) to the range allowed by the combined Fermi-LAT + XENON-1T region,  $20 \text{ GeV} \lesssim m_\chi \lesssim 40 \text{ GeV}$ , the final state options for the surviving parameter space are drastically limited to only include either the real, pure  $b\bar{b}$ , or a  $b\bar{b}/\tau^+\tau^-$  admixture.

The equivalent fit to Fermi-LAT mock data for BP2 is shown in Fig. 4(a). The signal in gamma rays constrains the mass to  $m_\chi \lesssim 800$  GeV. On the other hand, we have shown in Fig. 2(b)



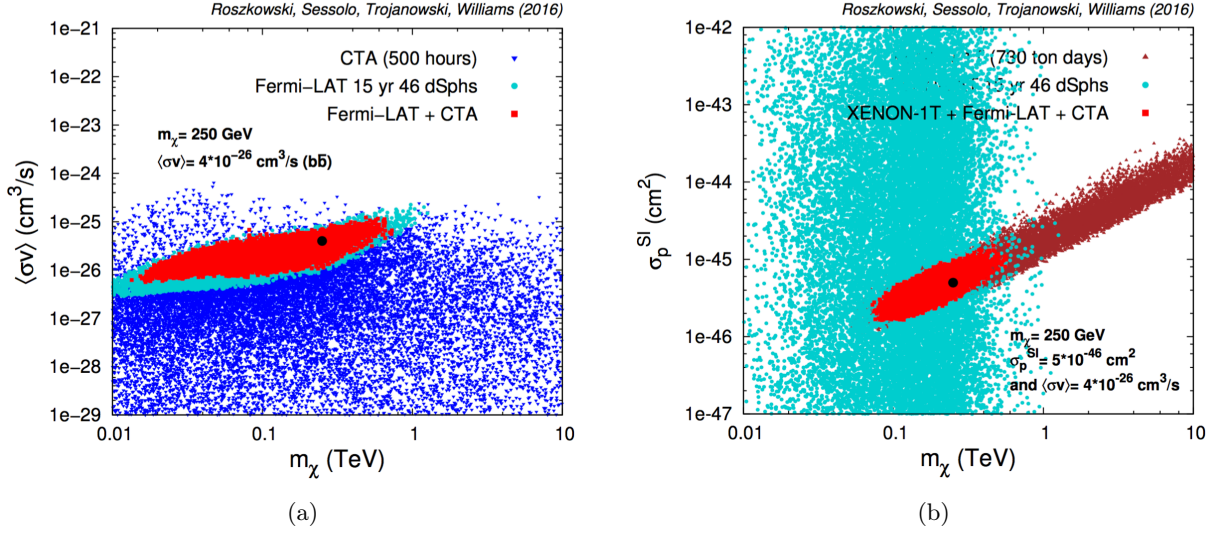


**Figure 5:** (a) Dark turquoise circles show the 95% C.L. fit to Fermi-LAT 15 yr 46 dSphs mock BP3 data in the  $(m_\chi, \sigma v)$  plane, blue upside-down triangles show the 95% C.L. reconstruction for the same point in CTA with 500 hours of observation, and the 95% C.L. combination of the two experiments is shown with red squares. (b) Same as Fig. 4(b) for BP3. Red squares show here the combination of Fermi-LAT, XENON-1T, and CTA.

that a hypothetical concurrent signal in one of the direct detection experiments would constrain the WIMP mass to  $m_\chi \gtrsim 40$  GeV. By projecting, for instance, the Fermi-LAT constrained region to the  $(m_\chi, \sigma_p^{SI})$  plane, one can visualize the combined 95% C.L. mass reconstruction region, whose lower bound is determined by XENON-1T and upper bound by Fermi-LAT dSphs. We show it with red squares in Fig. 4(b).

We can use the same technique to pinpoint the mass of BP3, characterized by  $m_\chi = 250$  GeV. The BP3 reconstructed region at Fermi-LAT 15 yr 46 dSphs, shown with dark turquoise circles in Fig. 5(a), presents the same qualitative features as for BP1 and BP2, as expected by construction. As was mentioned in Sec. 3, CTA’s sensitivity with approximately 500 hours of observation of the GC is expected for this mass to start closing in on the sensitivity expected at Fermi-LAT. In Fig. 5(a) we plot with blue down-pointing triangles the 95% C.L. reconstruction of BP3 in CTA. One can see that the resulting signal is too weak to provide any meaningful information. However, a combination of the Fermi-LAT and CTA likelihood functions shows for this point a slight improvement (red squares) on the mass reconstruction with respect to Fermi-LAT alone. This is a feature that is bound to become increasingly more pronounced as one considers larger DM mass.

The combined effect of Fermi-LAT, CTA, and XENON-1T data on the reconstruction of BP3 properties when one considers a concurrent observation in direct and indirect detection experiments is shown with red squares in Fig. 5(b).

We now move on to the 1000 GeV WIMP case that will allow us to investigate in detail how the considered uncertainties affect the mass and cross section reconstruction abilities of CTA. In Fig. 6 we present the case of BP4(a), featuring a 1 TeV WIMP with 100% branching ratio to  $b\bar{b}$  and  $\sigma v = 2 \times 10^{-25}$  cm<sup>3</sup>/s. We show the reconstructed 95% C.L. regions in the  $(m_\chi, \sigma v)$  plane in Fig. 6(a). Again, dark turquoise circles show the reconstruction in Fermi-LAT, blue triangles the reconstruction in CTA, whose precision is now much higher than for the previous benchmark



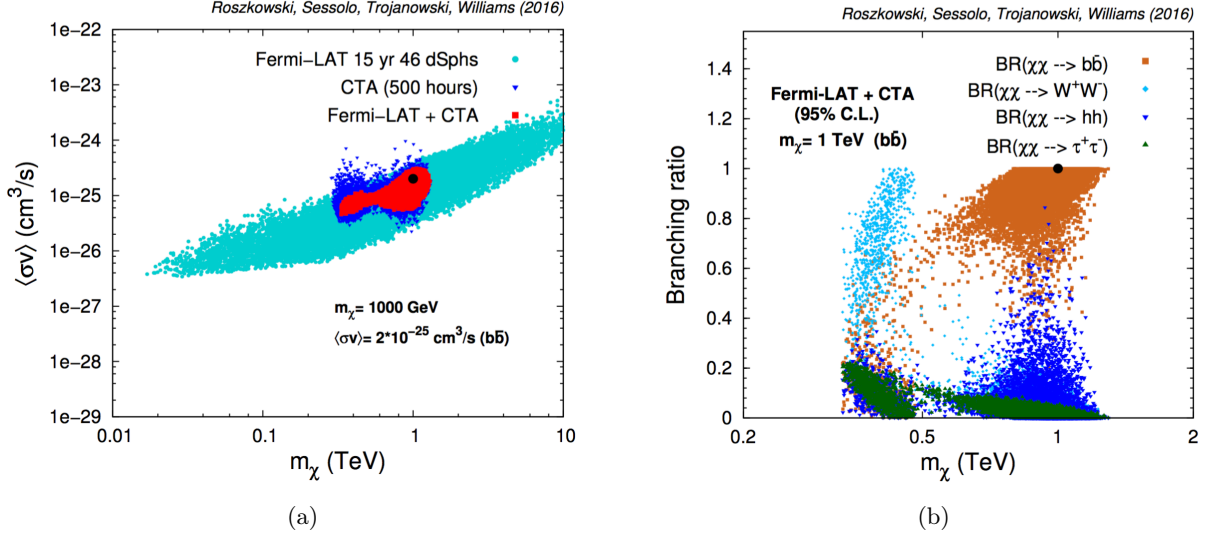


**Figure 6:** (a) Dark turquoise circles show the 95% C.L. fit in the  $(m_\chi, \sigma v)$  plane to Fermi-LAT 15 yr 46 dSphs mock BP4(a) data (the benchmark is shown in black). Blue upside-down triangles show the 95% C.L. fit for CTA 500 hours. The 95% C.L. combination of the two results in the  $(m_\chi, \sigma v)$  plane is shown with red squares. (b) The breakdown of the branching ratios to a particular annihilation final state versus the WIMP mass for the points of the 95% C.L. fit to Fermi-LAT + CTA data considered in (a). Light brown squares show the  $b\bar{b}$  branching ratio, dark green triangles the one to  $\tau^+\tau^-$ , deep-sky blue diamonds the one to  $W^+W^-$ , and blue upside-down triangles the one to  $hh$ .

points, and red squares the combined 95% C.L. region. Note how CTA can narrow down the mass range by almost two orders of magnitude with respect to Fermi-LAT alone, although substantial degeneracy among different reconstructed values of  $m_\chi$  and  $\sigma v$  remains.

Much of this degeneracy is due to the fact that the scan has the freedom to adjust the final state branching fraction of the DM candidate, giving a very similar energy spectrum, so that different options can equally fit in the wiggle room left by the large astrophysical and background uncertainties described in Sec. 2.2.2. This is shown in Fig. 6(b) where we plot the branching ratios to the 4 different final states considered here for the points that belong to the combined CTA + Fermi-LAT confidence region shown in Fig. 6(a). Interestingly, one can see that the data originating from a 1 TeV  $b\bar{b}$  benchmark point can be equally well fitted by that of a 400 – 500 GeV WIMP annihilating almost entirely to  $W^+W^-$  with a cross section  $\sigma v$  approximately 2 to 5 times smaller than the benchmark  $2 \times 10^{-25}$  cm<sup>3</sup>/s.

We pictorially translate the 95% C.L. uncertainty found in the  $(m_\chi, \sigma v)$  plane to an uncertainty in the gamma-ray fluxes in Fig. 7. Figure 7(a) shows the uncertainties in the reconstruction of BP1 spectra in Fermi-LAT, for the case that was presented in Fig. 3. The uncertainties, which we have assumed to be given by a combination of the uncertainty of the measurement of dSphs  $J$ -factors and the statistical Poisson uncertainty of the number of gamma-ray events from fluxes, can be shown as a light beige band allowing different shapes for  $dN_\gamma/dE \times \sigma v/m_\chi^2$ . The band can for instance accommodate at the same time the spectra for 13 GeV WIMPs annihilating into  $\tau^+\tau^-$ , 25 GeV WIMPs going to  $b\bar{b}$ , or 130 GeV WIMPs yielding predominantly  $W^+W^-$ . Note that Fig. 7(a) also pictorially shows how, for instance, the spectrum of a 75 GeV WIMP with 100% branching ratio

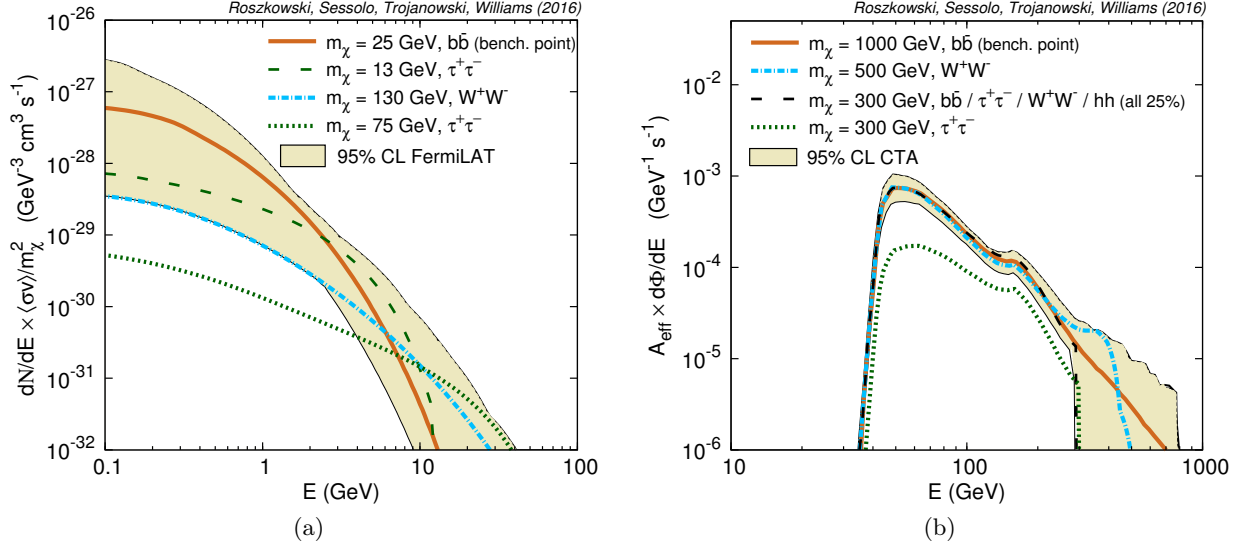


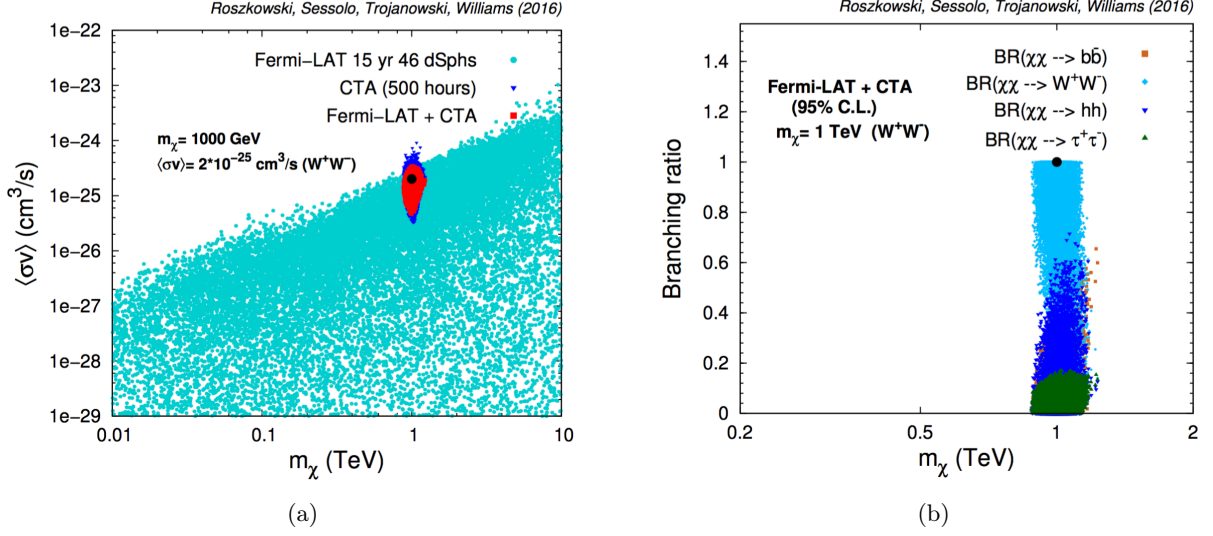
**Figure 7:** (a) A plot of several differential gamma-ray fluxes,  $dN_\gamma/dE \times \sigma v/m_\chi^2$ , that can fit the spectrum produced by BP1. The uncertainties around the reconstruction of the benchmark point spectrum in Fermi-LAT are shown with a light beige band. (b) Several effective gamma-ray fluxes,  $d\Phi/dE \times A_{\text{eff}}$ , that can fit the spectrum produced by BP4(a) in CTA. The uncertainties around the reconstruction of the benchmark point spectrum are shown with a light beige band.

into  $\tau^+\tau^-$  falls outside of the considered uncertainties, but that one could manage to bring it back into the allowed band by reducing the branching ratio to  $\tau^+\tau^-$  and at the same time increasing  $b\bar{b}$ , in agreement with what Fig. 3(b) shows.

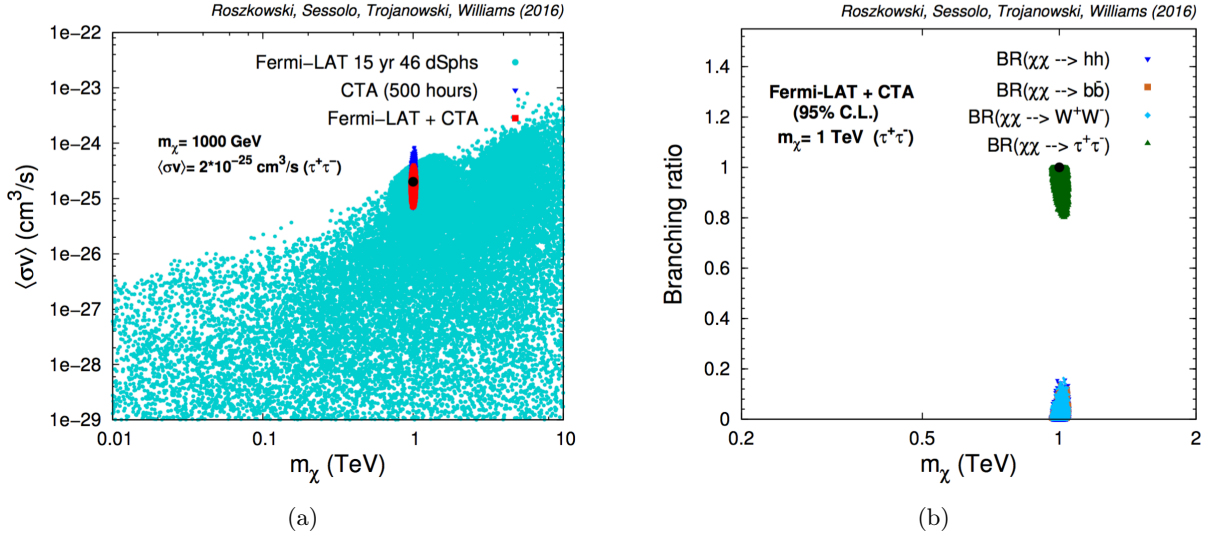
In Fig. 7(b) we show the case of BP4(a). The uncertainties of CTA can be translated into a light beige band about the gamma-ray flux times effective area, where the latter is responsible for effectively cutting out all signal in the bins with  $E < 30 \text{ GeV}$ . As one can see, the benchmark point spectrum corresponding to pure  $b\bar{b}$  final state and  $m_\chi = 1 \text{ TeV}$  can be mimicked over a wide range of energies. A  $\sim 500 \text{ GeV}$  DM particle annihilating into  $W^+W^-$  or, for even lower  $m_\chi$ , a DM particle annihilating into all four considered final states with branching ratios close to 25% can reproduce the same spectrum as BP4(a).

While the reconstruction in CTA of a point with the pure  $b\bar{b}$  final state is still lacking in precision and allows for degeneracies in mass and  $\sigma v$ , the same is not necessarily true if the benchmark point is characterized by a different final state. We present in Fig. 8(a) the reconstructed confidence regions for BP4(b), a point characterized by the same mass and  $\sigma v$  as BP4(a) but with final state 100%  $W^+W^-$ . Note that our projection of 15 yr 46 dSphs Fermi-LAT data does not show enough sensitivity to reconstruct a  $W^+W^-$  point with  $\sigma v = 2 \times 10^{-25} \text{ cm}^3/\text{s}$ , so that the 95% C.L. region (dark turquoise circles) does not provide useful information. However, CTA has a strong sensitivity to the features of a gamma-ray spectrum originating in a 1 TeV WIMP with 100% branching fraction to  $W^+W^-$ , especially because of a characteristic spectral “spike” appearing at about  $E \approx m_\chi$ , which has its origin in the splitting  $W^\pm \rightarrow W^\pm \gamma$  when  $E \gg M_W$  (see, e.g., [48]). The mass reconstruction becomes eventually very precise.

The final state can also be reconstructed very precisely for BP4(b), as is shown in Fig. 8(b), where one can see that the only allowed pure state is  $W^+W^-$  (deep-sky blue diamonds), although some 50% admixtures, especially with  $hh$  (dark blue down-pointing triangles) or  $b\bar{b}$  (light brown squares), are also possible.



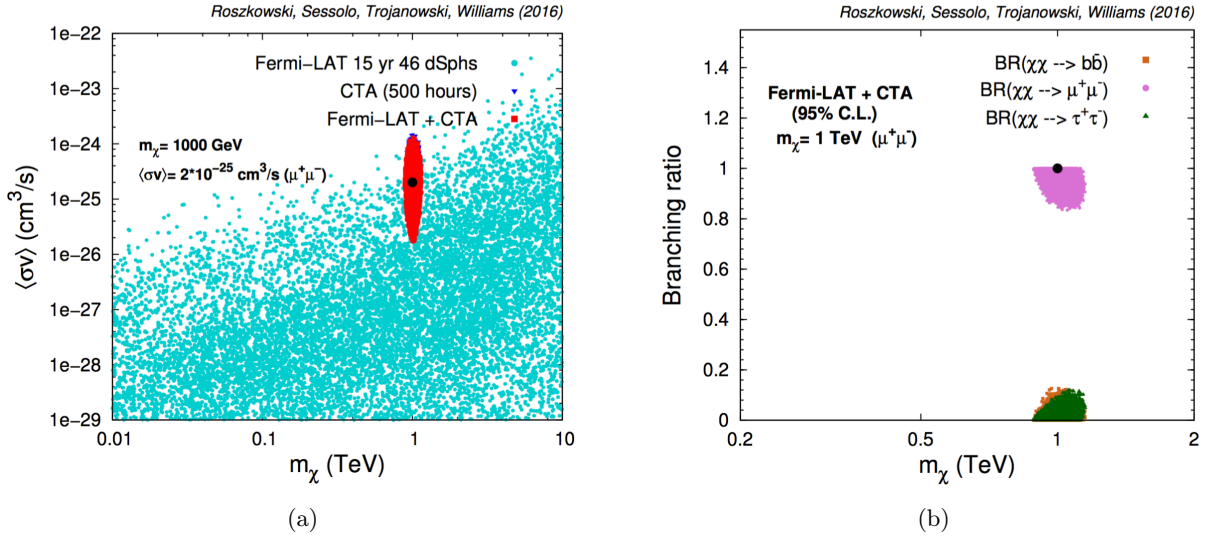
**Figure 8:** Same as Fig. 6, but for the benchmark BP4(b).



**Figure 9:** Same as Figs. 6 and 8, but for the benchmark BP4(c).

An analogous situation is encountered for BP4(c), characterized by a 1 TeV WIMP with 100%  $\tau^+\tau^-$  final state. The reconstruction is presented in Fig. 9(a). The CTA likelihood is responsible for the highly precise mass reconstruction, to which correspond an equally precise final state reconstruction, shown in Fig. 9(b).

We next move to the reconstruction of the gamma-ray spectra of purely leptonic origin. Consider the case of BP4(d), featuring a 1 TeV WIMP with the same  $\sigma v$  as the previous benchmark points and 100%  $\mu^+\mu^+$  final state. As was described in Sec. 3, we limit the final-state channels for this scan to 3: points are assumed to correspond to leptonic ( $\mu^+\mu^+$  final state), hadronic ( $b\bar{b}$ ), or mixed ( $\tau^+\tau^+$  and combinations) spectra. The reconstruction in the  $(m_\chi, \sigma v)$  plane is shown in



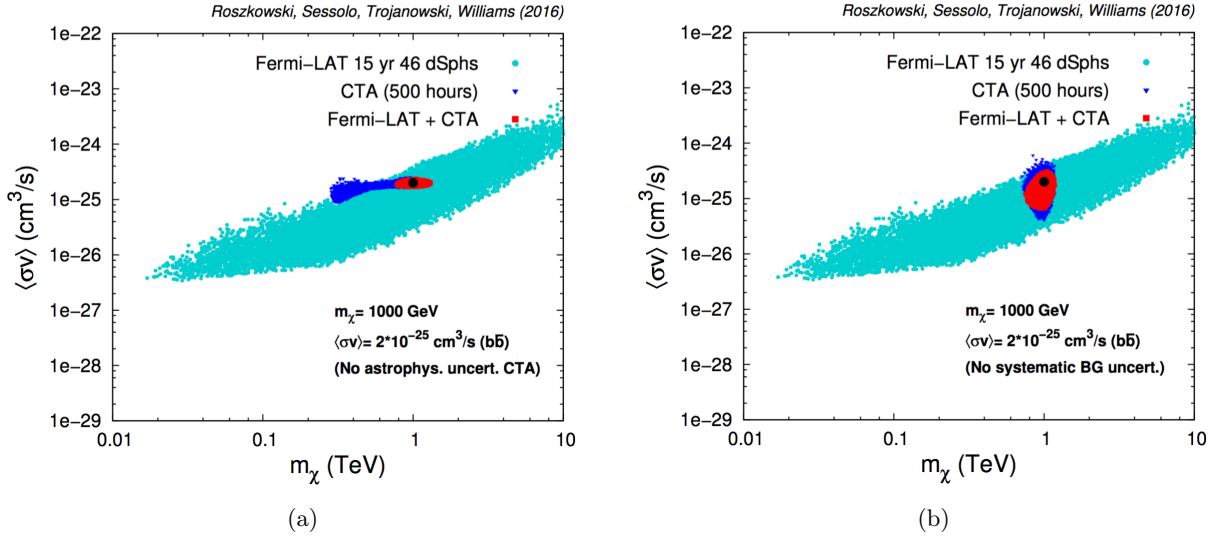
**Figure 10:** (a) Same as Fig. 6(a), but for the benchmark BP4(d). (b) The breakdown of the branching ratios to a particular annihilation final state versus the WIMP mass for the points of the 95% C.L. combination of FermiLAT and CTA data considered in (a). Light brown squares show the  $b\bar{b}$  branching ratio, dark green triangles the one to  $\tau^+\tau^-$ , and orchid circles the one to  $\mu^+\mu^-$ .

Fig. 10(a) and the final state reconstruction is shown in Fig. 10(b). Again the mass reconstruction is very good, although the weakness of the signal for the  $\mu^+\mu^+$  mode slightly spoils the reconstruction in  $\sigma v$ .

Finally, for BP5, characterized by  $m_\chi = 1000$  GeV, a canonical thermal  $\sigma v = 3 \times 10^{-26}$  cm<sup>3</sup>/s, and 100% branching ratio to  $W^+W^-$ , we found in our analysis that, with 500 hours of observation, CTA fairs relatively poorly (albeit better than Fermi-LAT 15 yr 46 dSphs) on the reconstruction of the WIMP mass or cross section, so that we do not present a plot for this case.

Given the excellent mass reconstruction reached in CTA for most benchmark points, we break down in Fig. 11 the effect of the different uncertainties that can spoil it. We are confronted with uncertainties of several kinds. There are astrophysical uncertainties, due to the unknown shape of the Galactic DM halo profile, which are included in our scans through the nuisance parameters  $\rho_0$  and  $\gamma_{\text{NFW}}$ . Note that the ranges considered in Table 3 for these parameters do not extend as much as to include less steep solutions [92, 93] for the halo profile, which are therefore neglected in this study. We then consider systematic uncertainties due the normalization of the isotropic cosmic-ray background and to the diffuse astrophysical gamma-ray background around the GC, parametrized, respectively, by the  $R_i^{\text{CR}}$  and  $R_i^{\text{GDE}}$  parameters in Eq. (2.13). We remind the reader that we have not included systematic uncertainties in the detector response [46].

In Fig. 11(a) we show the effect of neglecting the astrophysical uncertainties by setting the nuisance parameters to their central values when reconstructing BP4(a) in the  $(m_\chi, \sigma v)$  plane. When comparing to Fig. 6(a) one notices a significant improvement in the cross section reconstruction, not accompanied by an equally significant mass reconstruction improvement (the 95% C.L. region for CTA is indicated with blue upside-down triangles). This is due to the fact that the  $b\bar{b}$  spectrum for a  $\sim 1$  TeV WIMP and the  $W^+W^-$  spectrum for a  $\sim 500$  GeV WIMP are very similar, see Fig. 7(b). Our extension of the Ring Method effectively allows one to somewhat constrain the degrees of freedom associated with the  $R_i^{\text{CR}}$  and  $R_i^{\text{GDE}}$  parameters in Eq. (2.13) and, at the same



**Figure 11:** (a) The effect of neglecting the nuisance parameters when fitting for point BP4(a) in the  $(m_\chi, \sigma v)$  plane. The color code is the same as in Fig. 6(a). (b) The effect of neglecting the uncertainty in the  $R_i^{\text{CR}}$  and  $R_i^{\text{GDE}}$  parameters in Eq. (2.13) when fitting for BP4(a), compare Fig. 6(a).

time, the  $J$ -factors are in this scan fixed by construction. The strength of the signal, driven by  $\sigma v$ , is then also strongly constrained, but the remaining final state freedom introduces the residual uncertainty in the mass reconstruction.

In Fig. 11(b) we show instead the effect of setting  $R_i^{\text{CR}} = R_i^{\text{GDE}} = 1$  in Eq. (2.13), while maintaining the freedom to scan over the nuisance parameters. One can see the persistence of a small degeneracy between  $m_\chi = 1000$  GeV and some points with a smaller mass, characterized by a mixed final-state spectrum mimicking the features of a 1 TeV  $b\bar{b}$  case. The main uncertainty however is now in  $\sigma v$ , centered about the benchmark point. It is due to the fact that the signal depends on the product  $\sigma v/m_\chi^2 \times J$ , whose factors can be adjusted independently to produce a better fit.

As was mentioned in Sec. 2.2.2, our extension of the Ring Method plays an important role in reducing the background systematic uncertainties in CTA. In this paper we have presented results based on the 4 regions shown in Fig. 1. However, we also mentioned in Sec. 2.2.2 that what is really important is to perform the analysis in at least 3 spatial regions, as there are 3 separate components producing a signal in Eq. (2.13).

In Fig. 12 we present the 95% C.L. reconstruction regions at CTA for a progressively increasing number of regions. We show it for BP4(a) in Fig. 12(a) and for BP4(b) in Fig. 12(b). Marked with turquoise circles, one can see the reconstruction obtained using the traditional 2-region method of, e.g., [43–45, 47]. The region in violet triangles shows that most of the improvement can be obtained by adding one additional region to the Ring Method (3 regions result when Regions 1 and 2 in Fig. 1 are unified into a single patch). One can also see that adding the fourth region brings about a moderate additional improvement (dark blue upside-down triangles as in the other plots). It is important to point out that, as the uncertainties in the background normalization become increasingly constrained by adding additional regions in the sky, systematic uncertainties of the detector response, which we do not consider here, can become the dominant source.

In Fig. 13 we present the results of extending the exposure of CTA to 1000 hours of observation,



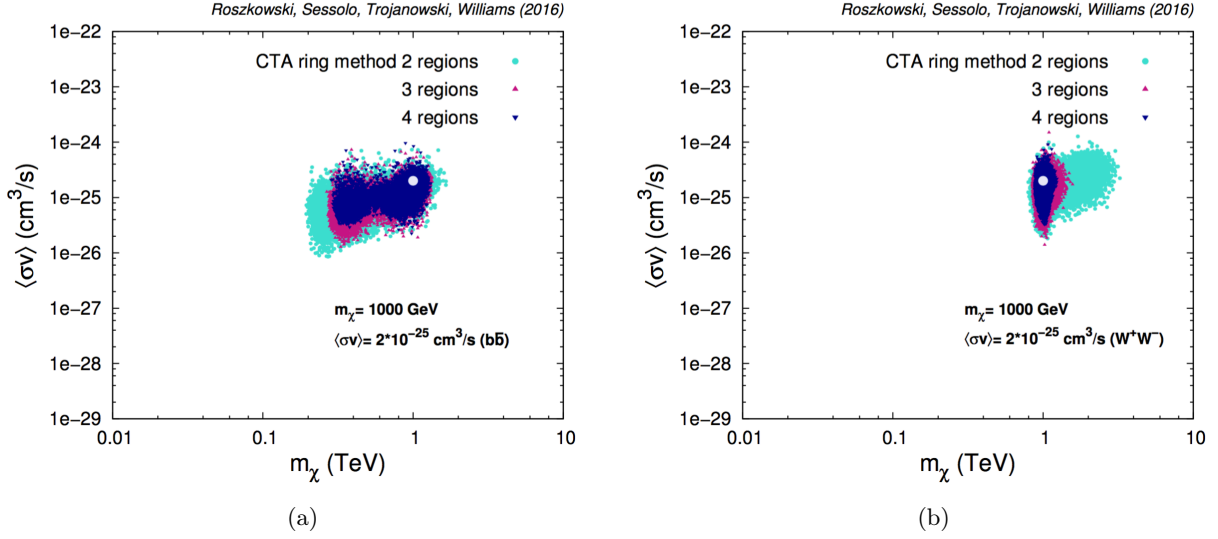


**Figure 12:** (a) Turquoise circles show the fit to CTA 500 hour mock BP4(a) data when considering the Ring Method with 2 spatial regions as, e.g., in Ref. [47]. Violet triangles show the fit when considering 3 regions in the sky, and dark blue upside-down triangles the fit with 4 regions, designed as in Fig. 1. (b) Same as (a) but for BP4(b).

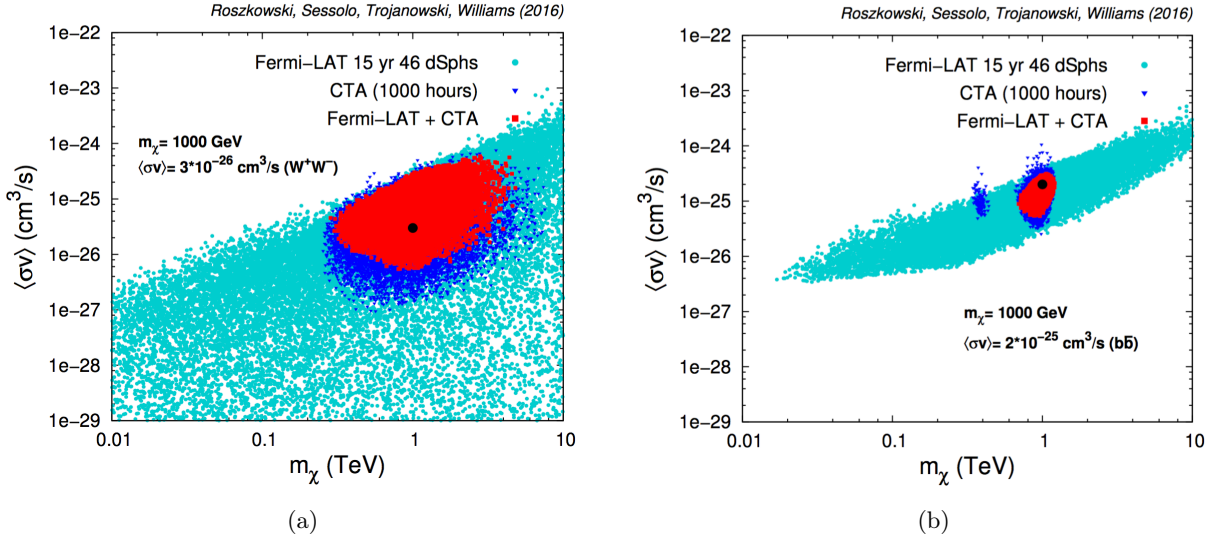


**Figure 13:** (a) Same as Fig. 6(a), but for the benchmark BP5, where the exposure of CTA has been extended to 1000 hours. (b) Same as (a) but for BP4(a), compare Fig. 6(a).

which could be possibly allocated in the optimistic case of a WIMP discovery. Specifically, the reconstruction would improve in the case of BP5, a point characterized by the canonical  $\sigma v = 3 \times 10^{-26} \text{ cm}^3/\text{s}$  for which the reconstruction with 500 hours was quite poor. One can see in Fig. 13(a) that even with increased exposure, this case remains tricky and lies at the borderline of the instrument reconstruction abilities, given the current state of uncertainties. We show for



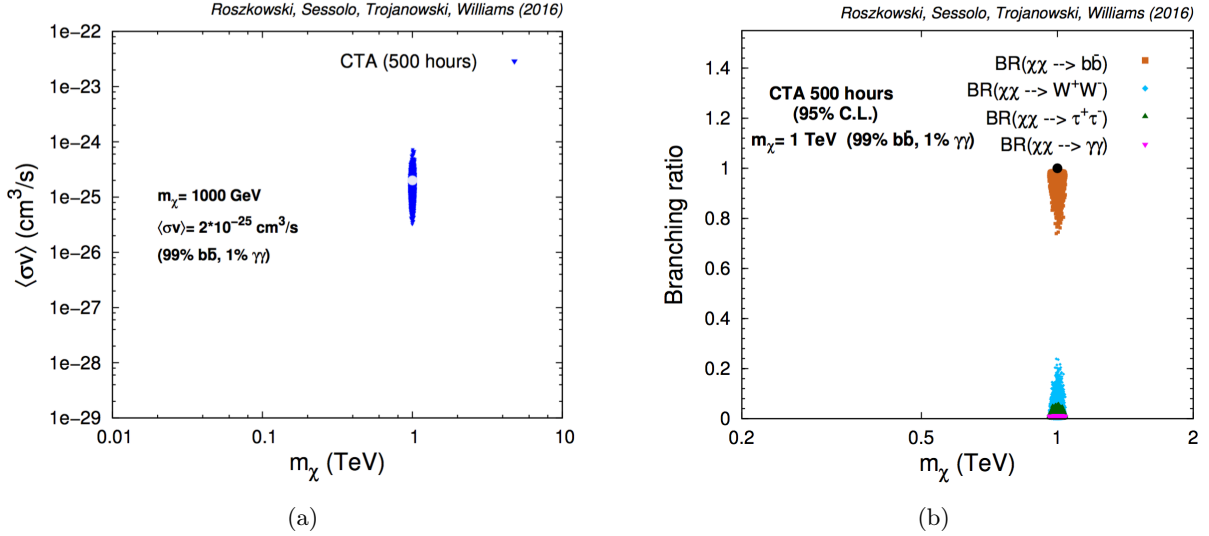


**Figure 14:** (a) The 95% C.L. CTA reconstructed region in the  $(m_\chi, \sigma v)$  plane for a point similar to BP4(a) but with  $\text{Br}(\chi\chi \rightarrow b\bar{b}) = 99\%$  and  $\text{Br}(\chi\chi \rightarrow \gamma\gamma) = 1\%$ , compare Fig. 6(a). (b) The breakdown of the reconstructed branching ratios for the points shown in (a).

completeness in Fig. 13(b) the reconstruction with 1000 hours in the case of BP4(a), with a larger  $\sigma v$ . The 95% C.L. combined region shrinks here significantly relative to Fig. 6(a).

We conclude this section by discussing in brief a few cases characterized by annihilation final states different from the ones described above. It was recently pointed out in [94] that gamma-ray telescopes could be sensitive to the  $\nu_\alpha\nu_\alpha$  annihilation final states for a cross section not much larger than the typical values considered here. We have explicitly checked numerically that, for a benchmark point characterized  $m_\chi = 1000$  GeV,  $\sigma v = 2 \times 10^{-25}$  cm<sup>3</sup>/s, and a 100% branching ratio to  $\nu_\tau\nu_\tau$ , our likelihood function for CTA cannot reconstruct the WIMP properties. By increasing  $\sigma v$ , some loose 95% C.L. contours in the  $(m_\chi, \sigma v)$  plane would start to appear for  $\sigma v > 5 \times 10^{-25}$  cm<sup>3</sup>/s.

On the other hand, CTA is expected to be very sensitive to even small branching ratios to the monochromatic  $\gamma\gamma$  final state. To give a feeling of how this effectively affects the reconstruction of WIMP properties at CTA, we present in Fig. 14(a) the 95% C.L. region in the  $(m_\chi, \sigma v)$  plane for the fit to a point similar to BP4(a) (see Fig. 6), but characterized by  $\text{Br}(\chi\chi \rightarrow b\bar{b}) = 99\%$  and  $\text{Br}(\chi\chi \rightarrow \gamma\gamma) = 1\%$ . One can see that even a small branching fraction to gamma-ray lines has the power to erase the mass degeneracy that appears in the case of 100%  $b\bar{b}$ , thus leaving behind only the significant uncertainty in the reconstruction of  $\sigma v$ , which is due to the unknown real value of the nuisance parameters, in particular  $\rho_0$ .

We show in Fig. 14(b) the breakdown of the reconstructed branching ratios for the points appearing in Fig. 14(a). One can see that  $\text{Br}(\chi\chi \rightarrow \gamma\gamma)$  in particular can be reconstructed to very good accuracy.

## 5 Summary and conclusions

In this work we addressed the issue of WIMP mass and cross section reconstruction in case a positive measurement of a DM signal is made in either an underground direct detection experiment or in a diffuse gamma radiation experiment, or both. For the former we considered the expected sensitivity

of XENON-1T, SuperCDMS-Snolab, and DarkSide-G2, while for the latter we considered projected 15 yr data from Fermi-LAT observation of 46 dSphs and projected CTA sensitivity to a signal from the Galactic Center assuming the default observation time of 500 hours. For each we built a likelihood function assuming realistic astrophysical uncertainties.

We considered eight WIMP cases (benchmark points) spanning a wide range of mass from 25 GeV up to 1 TeV and featuring  $\sigma_p^{\text{SI}}$  (direct detection) or  $\sigma v$  (gamma rays) large enough to be within the discovery reach of the above experiments. For  $\sigma v$  we further considered not only a “default” WIMP annihilation final state  $b\bar{b}$  but also  $\tau^+\tau^-$ ,  $W^+W^-$ , and  $\mu^+\mu^-$ . For each case we generated MC simulations of WIMP parameters producing in different experiments a signal within  $2\sigma$  of the considered benchmark point. We did not assume any specific particle physics model or scenario, and for this reason neither did we impose any collider limits nor the relic density constraint.

Our general conclusion is that, even in the optimistic cases of cross sections large enough to warrant a strong signal detection, reconstructing WIMP properties will for the most part be rather challenging. As previously shown, direct detection experiments will only be able to reconstruct WIMP mass below some 100 GeV, above which event spectra become basically degenerate. Gamma-ray energy spectra, on the other hand, are WIMP mass dependent but face another type of degeneracy related to different final states at different WIMP mass. This can severely limit the ability of Fermi-LAT, in the low mass regime, and, to a lesser extent, CTA, in the high mass regime, to determine WIMP mass,  $\sigma v$ , or annihilation final states, when considered alone.

However, we found that in several interesting cases a remarkable improvement in WIMP reconstruction can be achieved by combining discovery data from Fermi-LAT and/or CTA, or by combining gamma-ray observatories with direct detection experiments.

For example, at lower WIMP mass (c.f. 25 GeV), good mass determination in direct detection experiments may not only help substantially reduce the range of  $\sigma v$  allowed by a positive measurement at Fermi-LAT, but also severely restrict WIMP annihilation final states. At the other end of the considered WIMP mass range (1 TeV), best prospects come from CTA which will reach its maximum sensitivity there, while Fermi-LAT’s sensitivity will be poorer, but not always negligible. We showed that in the case of CTA one can engineer a simple extension of the Ring Method that provides significant reduction of the systematic uncertainties in the background normalization without the need of a full morphological analysis. We also quantified the improvement in the WIMP property reconstruction associated with increasing the allocated exposure over the default value of 500 hours.

While a signal in CTA would allow for a fairly crude ( $b\bar{b}$  final state), good ( $W^+W^-$ ) or even very good ( $\tau^+\tau^-$  and  $\mu^+\mu^-$ ) WIMP mass determination, combining it with an additional signal from Fermi-LAT may help reducing the range of  $\sigma v$  and the allowed branching fractions to different final states.

The most difficult mass range appears to be the middle range between some 100 GeV and a few hundred GeV where direct detection gives a very poor mass determination, Fermi-LAT starts losing more and more sensitivity with increasing WIMP mass, while that of CTA has not yet reached its full strength. However, even in this tricky parameter space region we have shown that in case of a concurrent detection in both a direct detection experiment and Fermi-LAT data, the former can set a lower bound on the WIMP mass and the latter an upper bound that can be combined together to give a rough reconstruction of the WIMP mass and scattering cross section.

In conclusion, while a detection of a DM signal will be a landmark achievement whose importance will be difficult to overemphasize, the determination of WIMP properties from a DM signal in one or more types of experiment is likely to be very challenging. However, a complementary approach using multiple experimental venues can, as is often the case, reduce the degeneracy and provide better information on the DM properties.

## Acknowledgments

We would like to thank Andrzej Hryczuk for helpful comments. The work of LR is supported by the Lancaster-Manchester-Sheffield Consortium for Fundamental Physics under STFC Grant No. ST/L000520/1. ST is supported in part by the National Science Centre, Poland, under research grant DEC-2014/13/N/ST2/02555 and by the Polish Ministry of Science and Higher Education under research grant 1309/MOB/IV/2015/0. The use of the CIS computer cluster at the National Centre for Nuclear Research is gratefully acknowledged.

## References

- [1] **LUX** Collaboration, D. S. Akerib et al., *First results from the LUX dark matter experiment at the Sanford Underground Research Facility*, *Phys. Rev. Lett.* **112** (2014) 091303, [[arXiv:1310.8214](#)].
- [2] **LUX** Collaboration, D. S. Akerib et al., *Improved Limits on Scattering of Weakly Interacting Massive Particles from Reanalysis of 2013 LUX Data*, *Phys. Rev. Lett.* **116** (2016), no. 16 161301, [[arXiv:1512.03506](#)].
- [3] **XENON100** Collaboration, E. Aprile et al., *Dark Matter Results from 225 Live Days of XENON100 Data*, *Phys. Rev. Lett.* **109** (2012) 181301, [[arXiv:1207.5988](#)].
- [4] **PICO** Collaboration, C. Amole et al., *Dark Matter Search Results from the PICO-60 CF<sub>3</sub>I Bubble Chamber*, *Submitted to: Phys. Rev. D* (2015) [[arXiv:1510.07754](#)].
- [5] **PICO** Collaboration, C. Amole et al., *Improved Dark Matter Search Results from PICO-2L Run-2*, *Submitted to: Phys. Rev. D* (2016) [[arXiv:1601.03729](#)].
- [6] **LUX** Collaboration, D. S. Akerib et al., *Results on the Spin-Dependent Scattering of Weakly Interacting Massive Particles on Nucleons from the Run 3 Data of the LUX Experiment*, *Phys. Rev. Lett.* **116** (2016), no. 16 161302, [[arXiv:1602.03489](#)].
- [7] **ANTARES** Collaboration, S. Adrian-Martinez et al., *First results on dark matter annihilation in the Sun using the ANTARES neutrino telescope*, *JCAP* **1311** (2013) 032, [[arXiv:1302.6516](#)].
- [8] **Super-Kamiokande** Collaboration, K. Choi et al., *Search for neutrinos from annihilation of captured low-mass dark matter particles in the sun by super-kamiokande*, *Phys. Rev. Lett.* **114** (Apr, 2015) 141301.
- [9] **IceCube** Collaboration, M. G. Aartsen et al., *Improved limits on dark matter annihilation in the Sun with the 79-string IceCube detector and implications for supersymmetry*, *JCAP* **1604** (2016), no. 04 022, [[arXiv:1601.00653](#)].
- [10] **Fermi-LAT** Collaboration, M. Ackermann et al., *Searching for Dark Matter Annihilation from Milky Way Dwarf Spheroidal Galaxies with Six Years of Fermi Large Area Telescope Data*, *Phys. Rev. Lett.* **115** (2015), no. 23 231301, [[arXiv:1503.02641](#)].
- [11] **HESS** Collaboration, A. Abramowski et al., *Search for a Dark Matter annihilation signal from the Galactic Center halo with H.E.S.S.*, *Phys. Rev. Lett.* **106** (2011) 161301, [[arXiv:1103.3266](#)].
- [12] A. M. Green, *Determining the WIMP mass from a single direct detection experiment, a more detailed study*, *JCAP* **0807** (2008) 005, [[arXiv:0805.1704](#)].
- [13] L. E. Strigari and R. Trotta, *Reconstructing WIMP Properties in Direct Detection Experiments Including Galactic Dark Matter Distribution Uncertainties*, *JCAP* **0911** (2009) 019, [[arXiv:0906.5361](#)].
- [14] M. Pato, L. Baudis, G. Bertone, R. Ruiz de Austri, L. E. Strigari, and R. Trotta, *Complementarity of Dark Matter Direct Detection Targets*, *Phys. Rev.* **D83** (2011) 083505, [[arXiv:1012.3458](#)].
- [15] M. Pato, L. E. Strigari, R. Trotta, and G. Bertone, *Taming astrophysical bias in direct dark matter searches*, *JCAP* **1302** (2013) 041, [[arXiv:1211.7063](#)].

- [16] Y.-T. Chou and C.-L. Shan, *Effects of Residue Background Events in Direct Dark Matter Detection Experiments on the Determination of the WIMP Mass*, *JCAP* **1008** (2010) 014, [[arXiv:1003.5277](#)].
- [17] C.-L. Shan, *Estimating the Spin-Independent WIMP-Nucleon Coupling from Direct Dark Matter Detection Data*, [arXiv:1103.0481](#).
- [18] C.-L. Shan, *Effects of Residue Background Events in Direct Dark Matter Detection Experiments on the Estimation of the Spin-Independent WIMP-Nucleon Coupling*, [arXiv:1103.4049](#).
- [19] B. J. Kavanagh and A. M. Green, *Improved determination of the WIMP mass from direct detection data*, *Phys. Rev.* **D86** (2012) 065027, [[arXiv:1207.2039](#)].
- [20] B. J. Kavanagh and A. M. Green, *Model independent determination of the dark matter mass from direct detection experiments*, *Phys. Rev. Lett.* **111** (2013), no. 3 031302, [[arXiv:1303.6868](#)].
- [21] A. H. G. Peter, V. Gluscevic, A. M. Green, B. J. Kavanagh, and S. K. Lee, *WIMP physics with ensembles of direct-detection experiments*, *Phys. Dark Univ.* **5-6** (2014) 45–74, [[arXiv:1310.7039](#)].
- [22] J. L. Newstead, T. D. Jacques, L. M. Krauss, J. B. Dent, and F. Ferrer, *Scientific reach of multiton-scale dark matter direct detection experiments*, *Phys. Rev.* **D88** (2013), no. 7 076011, [[arXiv:1306.3244](#)].
- [23] N. Bernal and S. Palomares-Ruiz, *Constraining Dark Matter Properties with Gamma-Rays from the Galactic Center with Fermi-LAT*, *Nucl. Phys.* **B857** (2012) 380–410, [[arXiv:1006.0477](#)].
- [24] N. Bernal and S. Palomares-Ruiz, *Constraining the Milky Way Dark Matter Density Profile with Gamma-Rays with Fermi-LAT*, *JCAP* **1201** (2012) 006, [[arXiv:1103.2377](#)].
- [25] S. Palomares-Ruiz and J. M. Siegal-Gaskins, *Annihilation vs. Decay: Constraining dark matter properties from a gamma-ray detection*, *JCAP* **1007** (2010) 023, [[arXiv:1003.1142](#)].
- [26] F. Calore, I. Cholis, and C. Weniger, *Background model systematics for the Fermi GeV excess*, *JCAP* **1503** (2015) 038, [[arXiv:1409.0042](#)].
- [27] N. Bernal, A. Goudelis, Y. Mambrini, and C. Munoz, *Determining the WIMP mass using the complementarity between direct and indirect searches and the ILC*, *JCAP* **0901** (2009) 046, [[arXiv:0804.1976](#)].
- [28] **XENON** Collaboration, E. Aprile et al., *Physics reach of the XENON1T dark matter experiment*, *Submitted to: JCAP* (2015) [[arXiv:1512.07501](#)].
- [29] C. Arina, G. Bertone, and H. Silverwood, *Complementarity of direct and indirect Dark Matter detection experiments*, *Phys. Rev.* **D88** (2013), no. 1 013002, [[arXiv:1304.5119](#)].
- [30] B. J. Kavanagh, M. Fornasa, and A. M. Green, *Probing WIMP particle physics and astrophysics with direct detection and neutrino telescope data*, *Phys. Rev.* **D91** (2015), no. 10 103533, [[arXiv:1410.8051](#)].
- [31] O. Mena, S. Palomares-Ruiz, and S. Pascoli, *Reconstructing WIMP properties with neutrino detectors*, *Phys. Lett.* **B664** (2008) 92–96, [[arXiv:0706.3909](#)].
- [32] C.-L. Shan, *Effects of Residue Background Events in Direct Dark Matter Detection Experiments on the Determinations of Ratios of WIMP-Nucleon Cross Sections*, [arXiv:1104.5305](#).
- [33] M. Pato, *What can(not) be measured with ton-scale dark matter direct detection experiments*, *JCAP* **1110** (2011) 035, [[arXiv:1106.0743](#)].
- [34] D. G. Cerde  so et al., *Complementarity of dark matter direct detection: the role of bolometric targets*, *JCAP* **1307** (2013) 028, [[arXiv:1304.1758](#)]. [Erratum: *JCAP*1309,E01(2013)].
- [35] B. Acharya, M. Actis, T. Aghajani, G. Agnetta, J. Aguilar, et al., *Introducing the CTA concept*, *Astropart.Phys.* **43** (2013) 3–18.
- [36] L. Roszkowski, E. M. Sessolo, and A. J. Williams, *What next for the CMSSM and the NUHM: Improved prospects for superpartner and dark matter detection*, *JHEP* **08** (2014) 067, [[arXiv:1405.4289](#)].

- [37] L. J. Hall and Y. Nomura, *Spread Supersymmetry*, *JHEP* **1201** (2012) 082, [[arXiv:1111.4519](#)].
- [38] A. Arvanitaki, N. Craig, S. Dimopoulos, and G. Villadoro, *Mini-Split*, *JHEP* **1302** (2013) 126, [[arXiv:1210.0555](#)].
- [39] L. J. Hall, Y. Nomura, and S. Shirai, *Spread Supersymmetry with Wino LSP: Gluino and Dark Matter Signals*, *JHEP* **1301** (2013) 036, [[arXiv:1210.2395](#)].
- [40] A. Hryczuk, I. Cholis, R. Iengo, M. Tavakoli, and P. Ullio, *Indirect Detection Analysis: Wino Dark Matter Case Study*, *JCAP* **1407** (2014) 031, [[arXiv:1401.6212](#)].
- [41] D. C. Malling et al., *After LUX: The LZ Program*, [arXiv:1110.0103](#).
- [42] **DarkSide** Collaboration, C. E. Aalseth et al., *The DarkSide Multiton Detector for the Direct Dark Matter Search*, *Adv. High Energy Phys.* **2015** (2015) 541362.
- [43] **CTA Consortium** Collaboration, M. Doro et al., *Dark Matter and Fundamental Physics with the Cherenkov Telescope Array*, *Astropart. Phys.* **43** (2013) 189–214, [[arXiv:1208.5356](#)].
- [44] M. Wood, J. Buckley, S. Digel, S. Funk, D. Nieto, and M. A. Sanchez-Conde, *Prospects for Indirect Detection of Dark Matter with CTA*, in *Community Summer Study 2013: Snowmass on the Mississippi (CSS2013) Minneapolis, MN, USA, July 29-August 6, 2013*, 2013. [arXiv:1305.0302](#).
- [45] M. Pierre, J. M. Siegal-Gaskins, and P. Scott, *Sensitivity of CTA to dark matter signals from the Galactic Center*, *JCAP* **1406** (2014) 024, [[arXiv:1401.7330](#)]. [Erratum: JCAP1410,E01(2014)].
- [46] H. Silverwood, C. Weniger, P. Scott, and G. Bertone, *A realistic assessment of the CTA sensitivity to dark matter annihilation*, *JCAP* **1503** (2015), no. 03 055, [[arXiv:1408.4131](#)].
- [47] L. Roszkowski, E. M. Sessolo, and A. J. Williams, *Prospects for dark matter searches in the pMSSM*, *JHEP* **02** (2015) 014, [[arXiv:1411.5214](#)].
- [48] V. Lefranc, E. Moulin, P. Panci, and J. Silk, *Prospects for Annihilating Dark Matter in the inner Galactic halo by the Cherenkov Telescope Array*, *Phys. Rev.* **D91** (2015), no. 12 122003, [[arXiv:1502.05064](#)].
- [49] **CTA Consortium** Collaboration, J. Carr et al., *Prospects for Indirect Dark Matter Searches with the Cherenkov Telescope Array (CTA)*, in *Proceedings, 34th International Cosmic Ray Conference (ICRC 2015)*, 2015. [arXiv:1508.06128](#).
- [50] L. Goodenough and D. Hooper, *Possible Evidence For Dark Matter Annihilation In The Inner Milky Way From The Fermi Gamma Ray Space Telescope*, [arXiv:0910.2998](#).
- [51] D. Hooper and L. Goodenough, *Dark Matter Annihilation in The Galactic Center As Seen by the Fermi Gamma Ray Space Telescope*, *Phys. Lett.* **B697** (2011) 412–428, [[arXiv:1010.2752](#)].
- [52] R. Bartels, S. Krishnamurthy, and C. Weniger, *Strong support for the millisecond pulsar origin of the Galactic center GeV excess*, *Phys. Rev. Lett.* **116** (2016), no. 5 051102, [[arXiv:1506.05104](#)].
- [53] P. Agrawal, B. Batell, P. J. Fox, and R. Harnik, *WIMPs at the Galactic Center*, *JCAP* **1505** (2015) 011, [[arXiv:1411.2592](#)].
- [54] F. Calore, I. Cholis, C. McCabe, and C. Weniger, *A Tale of Tails: Dark Matter Interpretations of the Fermi GeV Excess in Light of Background Model Systematics*, *Phys. Rev.* **D91** (2015), no. 6 063003, [[arXiv:1411.4647](#)].
- [55] A. Achterberg, S. Amoroso, S. Caron, L. Hendriks, R. Ruiz de Austri, and C. Weniger, *A description of the Galactic Center excess in the Minimal Supersymmetric Standard Model*, *JCAP* **1508** (2015), no. 08 006, [[arXiv:1502.05703](#)].
- [56] T. Gherghetta, B. von Harling, A. D. Medina, M. A. Schmidt, and T. Trott, *SUSY implications from WIMP annihilation into scalars at the Galactic Center*, *Phys. Rev.* **D91** (2015) 105004, [[arXiv:1502.07173](#)].



- [57] G. Bertone, F. Calore, S. Caron, R. Ruiz, J. S. Kim, R. Trotta, and C. Weniger, *Global analysis of the  $p$ MSSM in light of the Fermi GeV excess: prospects for the LHC Run-II and astroparticle experiments*, *JCAP* **1604** (2016), no. 04 037, [[arXiv:1507.07008](#)].
- [58] M. Vogelsberger, A. Helmi, V. Springel, S. D. M. White, J. Wang, C. S. Frenk, A. Jenkins, A. D. Ludlow, and J. F. Navarro, *Phase-space structure in the local dark matter distribution and its signature in direct detection experiments*, *Mon. Not. Roy. Astron. Soc.* **395** (2009) 797–811, [[arXiv:0812.0362](#)].
- [59] F. S. Ling, E. Nezri, E. Athanassoula, and R. Teyssier, *Dark Matter Direct Detection Signals inferred from a Cosmological N-body Simulation with Baryons*, *JCAP* **1002** (2010) 012, [[arXiv:0909.2028](#)].
- [60] M. Weber and W. de Boer, *Determination of the local dark matter density in our Galaxy*, *Astron. Astrophys.* **509** (Jan., 2010) A25, [[arXiv:0910.4272](#)].
- [61] R. Catena and P. Ullio, *The local dark matter phase-space density and impact on WIMP direct detection*, *JCAP* **1205** (2012) 005, [[arXiv:1111.3556](#)].
- [62] A. Siebert, *Status and results from the RAVE survey*, in *SF2A-2012: Proceedings of the Annual meeting of the French Society of Astronomy and Astrophysics* (S. Boissier, P. de Laverny, N. Nardetto, R. Samadi, D. Valls-Gabaud, and H. Wozniak, eds.), pp. 121–127, Dec., 2012. [[arXiv:1210.0363](#)].
- [63] L. Hernquist, *An analytical model for spherical galaxies and bulges*, *Astrophys. J.* **356** (June, 1990) 359–364.
- [64] J. F. Navarro, C. S. Frenk, and S. D. M. White, *The Structure of cold dark matter halos*, *Astrophys. J.* **462** (1996) 563–575, [[astro-ph/9508025](#)].
- [65] A. Burkert, *The Structure of dark matter halos in dwarf galaxies*, *IAU Symp.* **171** (1996) 175, [[astro-ph/9504041](#)]. [*Astrophys. J.* 447, L25 (1995)].
- [66] J. Einasto, *Dark Matter*, in *Astronomy and Astrophysics 2010*, [Eds. Oddbjorn Engvold, Rolf Stabell, Bozena Czerny, John Lattanzio], in *Encyclopedia of Life Support Systems (EOLSS)*, Developed under the Auspices of the UNESCO, Eolss Publishers, Oxford, UK, 2009. [[arXiv:0901.0632](#)].
- [67] A. W. Graham, D. Merritt, B. Moore, J. Diemand, and B. Terzic, *Empirical models for Dark Matter Halos. I. Nonparametric Construction of Density Profiles and Comparison with Parametric Models*, *Astron. J.* **132** (2006) 2685–2700, [[astro-ph/0509417](#)].
- [68] **DarkSide** Collaboration, P. Agnes et al., *First Results from the DarkSide-50 Dark Matter Experiment at Laboratori Nazionali del Gran Sasso*, *Phys. Lett.* **B743** (2015) 456–466, [[arXiv:1410.0653](#)].
- [69] **CDMS-II** Collaboration, P. L. Brink et al., *Beyond the CDMS-II dark matter search: SuperCDMS*, *eConf* **C041213** (2004) 2529, [[astro-ph/0503583](#)].
- [70] M. Kuhlen, N. Weiner, J. Diemand, P. Madau, B. Moore, D. Potter, J. Stadel, and M. Zemp, *Dark Matter Direct Detection with Non-Maxwellian Velocity Structure*, *JCAP* **1002** (2010) 030, [[arXiv:0912.2358](#)].
- [71] C. McCabe, *The Astrophysical Uncertainties Of Dark Matter Direct Detection Experiments*, *Phys. Rev.* **D82** (2010) 023530, [[arXiv:1005.0579](#)].
- [72] A. M. Green, *Dependence of direct detection signals on the WIMP velocity distribution*, *JCAP* **1010** (2010) 034, [[arXiv:1009.0916](#)].
- [73] C. Stenge, R. Trotta, G. Bertone, A. H. G. Peter, and P. Scott, *Fundamental statistical limitations of future dark matter direct detection experiments*, *Phys. Rev.* **D86** (2012) 023507, [[arXiv:1201.3631](#)].
- [74] M. G. Walker, M. Mateo, E. W. Olszewski, J. Peñarrubia, N. Wyn Evans, and G. Gilmore, *A Universal Mass Profile for Dwarf Spheroidal Galaxies?*, *Astrophys. J.* **704** (Oct., 2009) 1274–1287, [[arXiv:0906.0341](#)].
- [75] J. Wolf, G. D. Martinez, J. S. Bullock, M. Kaplinghat, M. Geha, R. R. Muñoz, J. D. Simon, and F. F. Avedo, *Accurate masses for dispersion-supported galaxies*, *Month. Not. R. A. S.* **406** (Aug., 2010) 1220–1237, [[arXiv:0908.2995](#)].



- [76] G. D. Martinez, *A robust determination of Milky Way satellite properties using hierarchical mass modelling*, *Month.Not.R.A.S.* **451** (Aug., 2015) 2524–2535, [[arXiv:1309.2641](#)].
- [77] **Fermi-LAT** Collaboration, M. Ackermann et al., *Dark matter constraints from observations of 25 Milky Way satellite galaxies with the Fermi Large Area Telescope*, *Phys. Rev.* **D89** (2014) 042001, [[arXiv:1310.0828](#)].
- [78] M. Cirelli, G. Corcella, A. Hektor, G. Hutsi, M. Kadastik, P. Panci, M. Raidal, F. Sala, and A. Strumia, *PPPC 4 DM ID: A Poor Particle Physicist Cookbook for Dark Matter Indirect Detection*, *JCAP* **1103** (2011) 051, [[arXiv:1012.4515](#)]. [Erratum: JCAP1210,E01(2012)].
- [79] <http://fermi.gsfc.nasa.gov/ssc/data/access/lat/BackgroundModels.html>.
- [80] <http://fermi.gsfc.nasa.gov/ssc/data/analysis/software>.
- [81] <https://portal.cta-observatory.org/Pages/CTA-Performance.aspx>.
- [82] M. Ackermann et al., *Fermi-LAT Observations of the Diffuse  $\gamma$ -Ray Emission: Implications for Cosmic Rays and the Interstellar Medium*, *Astrophys.J.* **750** (May, 2012) 3, [[arXiv:1202.4039](#)].
- [83] **Fermi-LAT** Collaboration, M. Ackermann et al., *The spectrum of isotropic diffuse gamma-ray emission between 100 MeV and 820 GeV*, *Astrophys. J.* **799** (2015) 86, [[arXiv:1410.3696](#)].
- [84] **Fermi-LAT, MAGIC** Collaboration, M. L. Ahnen et al., *Limits to dark matter annihilation cross-section from a combined analysis of MAGIC and Fermi-LAT observations of dwarf satellite galaxies*, *JCAP* **1602** (2016), no. 02 039, [[arXiv:1601.06590](#)].
- [85] A. Goudelis, B. Herrmann, and O. StÃl, *Dark matter in the Inert Doublet Model after the discovery of a Higgs-like boson at the LHC*, *JHEP* **09** (2013) 106, [[arXiv:1303.3010](#)].
- [86] J. Sander et al., *SuperCDMS status from Soudan and plans for SNOLab*, *AIP Conf. Proc.* **1534** (2012) 129–135.
- [87] **SuperCDMS** Collaboration, P. L. Brink, *Conceptual Design for SuperCDMS SNOLAB*, *J. Low. Temp. Phys.* **167** (2012) 1093–1098.
- [88] F. Feroz, M. Hobson, and M. Bridges, *MultiNest: an efficient and robust Bayesian inference tool for cosmology and particle physics*, *Mon.Not.Roy.Astron.Soc.* **398** (2009) 1601–1614, [[arXiv:0809.3437](#)].
- [89] G. Belanger, F. Boudjema, A. Pukhov, and A. Semenov, *micrOMEGAs 3: A program for calculating dark matter observables*, *Comput.Phys.Commun.* **185** (2014) 960–985, [[arXiv:1305.0237](#)].
- [90] P. Ciafaloni, D. Comelli, A. Riotto, F. Sala, A. Strumia, and A. Urbano, *Weak Corrections are Relevant for Dark Matter Indirect Detection*, *JCAP* **1103** (2011) 019, [[arXiv:1009.0224](#)].
- [91] J. Buch, M. Cirelli, G. Giesen, and M. Taoso, *PPPC 4 DM secondary: A Poor Particle Physicist Cookbook for secondary radiation from Dark Matter*, *JCAP* **1509** (2015), no. 09 037, [[arXiv:1505.01049](#)].
- [92] P. Salucci, A. Lapi, C. Tonini, G. Gentile, I. Yegorova, et al., *The Universal Rotation Curve of Spiral Galaxies. 2. The Dark Matter Distribution out to the Virial Radius*, *Mon.Not.Roy.Astron.Soc.* **378** (2007) 41–47, [[astro-ph/0703115](#)].
- [93] F. Nesti and P. Salucci, *The Dark Matter halo of the Milky Way, AD 2013*, *JCAP* **1307** (2013) 016, [[arXiv:1304.5127](#)].
- [94] F. S. Queiroz, C. E. Yaguna, and C. Weniger, *Gamma-ray Limits on Neutrino Lines*, *JCAP* **1605** (2016), no. 05 050, [[arXiv:1602.05966](#)].